

Interplay of RhoA and mechanical forces in collective cell migration driven by leader cells

M. Reffay^{1,2}, M. C. Parrini³, O. Cochet-Escartin¹, B. Ladoux^{2,4}, A. Buguin¹, S. Coscoy¹, F. Amblard¹, J. Camonis^{3,5} and P. Silberzan^{1,5}

The leading front of a collectively migrating epithelium often destabilizes into multicellular migration fingers where a cell initially similar to the others becomes a leader cell while its neighbours do not alter. The determinants of these leader cells include mechanical and biochemical cues, often under the control of small GTPases. However, an accurate dynamic cartography of both mechanical and biochemical activities remains to be established. Here, by mapping the mechanical traction forces exerted on the surface by MDCK migration fingers, we show that these structures are mechanical global entities with the leader cells exerting a large traction force. Moreover, the spatial distribution of RhoA differential activity at the basal plane strikingly mirrors this force cartography. We propose that RhoA controls the development of these fingers through mechanical cues: the leader cell drags the structure and the peripheral pluricellular acto-myosin cable prevents the initiation of new leader cells.

When cells of an epithelium are presented *in vitro* with a free surface—created, for example, by a wound¹ or by the release of a physical barrier²—they migrate collectively while still maintaining strong cell–cell adhesions. This collective migration^{3,4}, characterized by coordinated long-range displacements within the monolayer, often coexists with a strong fingering of the leading edge where the pluricellular migration fingers are preceded by leader cells^{2,5,6}. Interestingly, similar structures are also observed *in vivo* in diverse situations such as morphogenesis¹ or cancer invasion^{7,8}.

At the start of migration, a cell initially similar to the others changes its phenotype into a ‘leader cell’. Its neighbours at the border do not undergo this transformation, and thus long migration fingers develop. The initiation of the leader cell is determined by mechanical cues resulting from, and acting on, intracellular biochemical activities^{9,10}. Of particular interest in this context is the distribution of the mechanical traction forces within these fingers and at the leader cell, and the coordination of these forces and the local biochemical activity of GTPases such as RhoA and Rac1. In contrast to single-cell migration, the mechanics of collective migration has been investigated only in the past few years^{11–14}. Similarly, the roles of RhoA and Rac1—whose importance in single-cell motility^{15,16} and in cell mechanics¹⁷ has long been recognized—have only recently been explored in more collective processes such as embryogenesis-related

collective migration^{18,19}, invasion from tumours²⁰ and wound-healing assays^{9,21}.

In this study, we directly investigated the correlation between GTPase activity and the mechanical forces in migration fingers by mapping in parallel the traction forces developed on the surface by the cells that constitute these structures and the local activity of RhoA and Rac1 in these cells. The experiments were conducted with epithelial Madin–Darby canine kidney (MDCK) cells using the ‘model wound assay’, in which cells are cultured in the apertures of micro-stencils. Peeling off these stencils triggers migration and finger formation without damaging the cells² (Supplementary Fig. 1A, B). Forces were then dynamically mapped using a dense array of soft micro-pillars as the underlying substrate, with each pillar acting as an independent force sensor²². The local activities of RhoA and Rac1 were measured at the basal plane of live cells transfected with the appropriate fluorescence resonance energy transfer (FRET)-based biosensor²³.

RESULTS

Migration fingers are mechanical global entities

As previously reported², fingers began to form two hours after the start of the experiments. Traction forces were measured in well-formed, long, mature structures (length d_0 , $40\ \mu\text{m} < d_0 < 100\ \mu\text{m}$,

¹Laboratoire Physico-chimie Curie—UMR 168, Institut Curie, Centre de Recherche, CNRS, UPMC, Paris, F-75248, France. ²Laboratoire Matière et Systèmes Complexes—UMR 7057, Université Paris Diderot, CNRS, Paris, F-75251, France. ³Analysis of Transduction Pathways Group—U830, Institut Curie, Centre de Recherche, Inserm, Paris, F-75248, France. ⁴Present address: Institut Jacques Monod (IJM), CNRS UMR 7592 & Université Paris Diderot, Paris F75205, France and Mechanobiology Institute, National University of Singapore 117411, Singapore.

⁵Correspondence should be addressed to J.C. or P.S. (e-mail: jacques.camonis@curie.fr or pascal.silberzan@curie.fr)

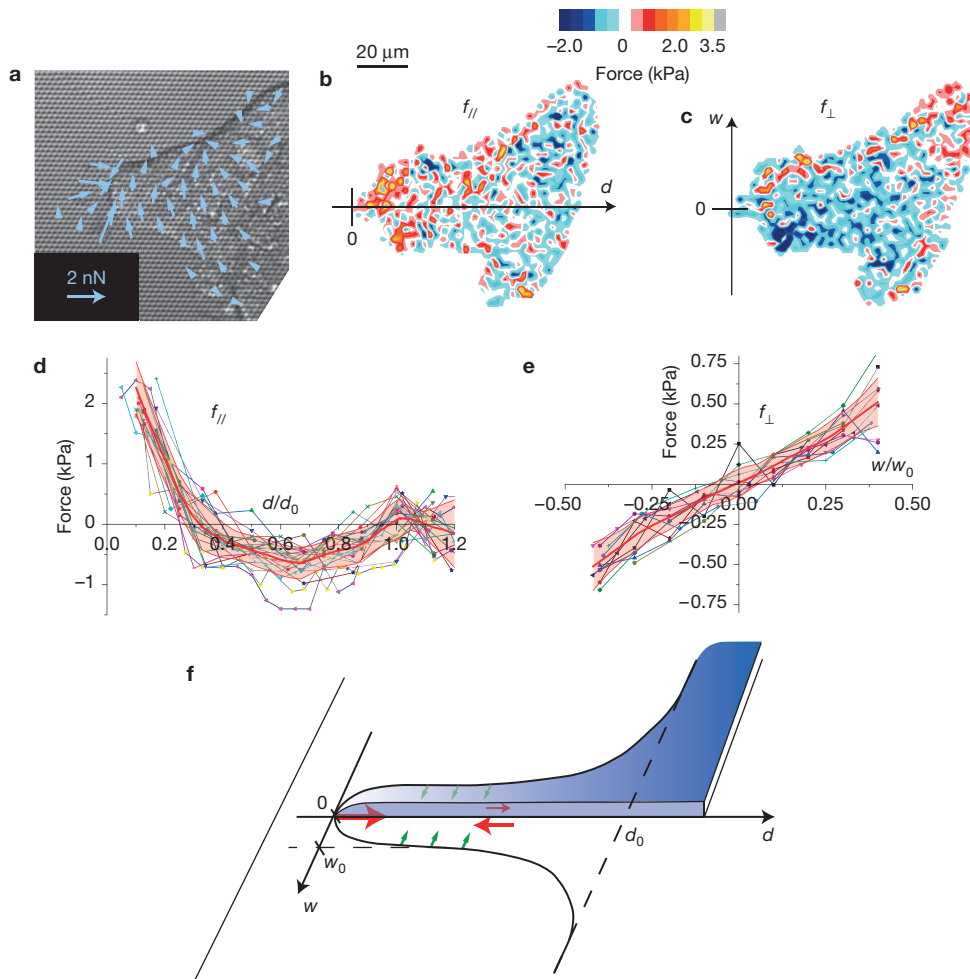


Figure 1 Traction forces exerted on the surface by the migration fingers. (a–c) Mapping of the traction forces obtained by the micro-pillar technique (a) and intensity of the projected component in the longitudinal (b) and transverse (c) directions. Only a fraction of the forces has been represented in a for clarity (representative images, replicated more than 20 times). (d,e) Force profiles in the parallel and perpendicular directions resulting from averaging forces for 22 and 12 fingers from 15 and 10

independent experiments respectively. The thick red line is the average profile, the coloured area represents the standard deviation. (f) Schematic representation of the direction of the forces: the leader cell exerts a stable traction longitudinal force whereas the forces in the fingers are highly dynamic and can be positive or negative (red arrows). The side edges exert a centripetal force (green arrows). Fingers were composed of typically 30 cells.

Fig. 1a) and were decomposed into two orthogonal components: parallel (longitudinal; $f_{||}$) and perpendicular (transverse; f_{\perp}) to the finger axis (Fig. 1b,c).

In Fig. 1d,e the longitudinal and transverse force profiles obtained through the analysis of these maps were normalized by the fingers' length (d_0) and width (w_0), respectively. The longitudinal force $f_{||}$ (Fig. 1d) at the tip was very large and positive (that is, directed from the tip of the finger towards its base (Fig. 1f)) but became negative within a couple of cell rows. The large pulling traction forces exerted by the leader cell could locally reach more than 2 kPa corresponding to a total integrated force of 40 nN under the lamella, where actin co-localizes with the phosphorylated active form of myosin²⁴ (Fig. 2a–c). These forces were greater than the average value measured at the edge of a growing epithelium on a low-rigidity substrate¹². Within the fingers, traction forces were highly dynamic and mostly localized at the cell–cell junctions²². They could locally be positive or negative, meaning that the cells forming

these structures move actively within them^{14,25}. When averaged out, $f_{||}$ was negative for $0.3 \cdot d_0 < d < d_0$, corresponding to an effective friction, with a minimum for $d \approx 0.7 \cdot d_0$ (Fig. 1d). Remarkably, as classically observed in single cells²⁶, the measured forces were proportional to the effective substrate rigidity in the 1–20 kPa range (Supplementary Fig. 1C,D).

The forces f_{\perp} perpendicular to the finger direction were greatest at the two borders and overall directed towards its centre, so that both sides of the fingers were, on average, balanced (Fig. 1e). They did not show significant variations along the finger principal direction and were lower than the maximal longitudinal forces (up to ~ 1 kPa; Fig. 1e). The spatial distribution of the observed forces in the fingers is summarized in Fig. 1f.

The distribution of forces at the tissue scale is reminiscent of migrating single cells such as fibroblasts²⁷ or keratocytes^{28,29}, meaning that the finger progresses on the surface as a global mechanical entity in which forces are transmitted from cell to cell to produce

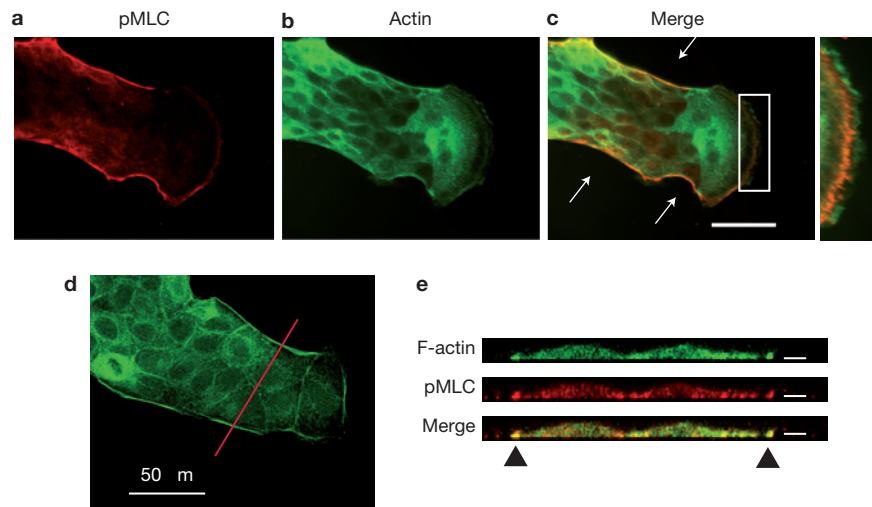


Figure 2 Presence of pluricellular acto-myosin structures at the fingers. (a–c) Phosphorylated myosin light chain (pMLC; immunofluorescence micrograph, a) and GFP-actin (b) co-localize at the scale of the finger in the form of a pluricellular acto-myosin cable (arrows) and at the leader lamella (zoom; c).

Scale bar: 50 μm . (d,e) Confocal section of a fixed finger showing the co-localization of F-actin and pMLC in the basal plane at the cable (triangles). The red line depicts the section plane. Scale bars of the x - z sections: 5 μm . (Representative images, 5 replicates.)

a coordinated motion^{12,14}. This directly confirms the concept of a mechanically self-consistent ‘super-cell’ as originally proposed in ref. 10.

The distribution of the transverse forces could be related to the presence of a pluricellular tensile acto-myosin cable along the edges of the finger and that localizes at the basal side of the structure^{9,30} (Fig. 2a–e). Indeed, when this cable was cut by photoablation-induced nanosurgery, it retracted in typically 30 s (Fig. 3a and Supplementary Fig. 2A,B and Supplementary Movie 1). Severing the cable also induced the displacement of nearby intracellular structures and triggered the relaxation of pillars along the cable but not directly at the cut (Fig. 3a and Supplementary Fig. 2C). Therefore, the actin cable is under tension³¹ similar to what is observed at the dorsal closure of the *Drosophila* embryo³², and interacts directly with the underlying substrate.

Furthermore, severing the cable led to the nucleation of a new leader cell at the precise location of the cut in a large fraction ($\sim 60\%$) of the experiments ($n = 22$; Fig. 3b and Supplementary Movie 2). An analysis of the velocity field within these newly formed structures unambiguously identified them as migration fingers (Fig. 3c). In the absence of external perturbation, new fingers also spontaneously initiated at ‘weak points’ in the cable as characterized by their lower green fluorescent protein (GFP)-actin fluorescence, as they developed their characteristic force profile (16 positive observations on 17 nascent fingers in 3 different experiments; Supplementary Fig. 3A). These data point to a ‘confining’ role for the acto-myosin cable, whose stored tension mechanically prevents the initiation of new leader cells and therefore allows the development of long fingers.

GTPases activities are distributed along the fingers

We also assessed GTPase activity during collective migration through the use of specific inhibitors: Y27632, which inhibits the action of ROCK downstream of Rho; blebbistatin, which targets the action of the myosins; and C3 transferase, which acts directly on Rho.

None of these inhibitors prevented migration but they all inhibited the formation of well-formed fingers, as did short interfering RNAs (siRNAs) targeting RhoA (Fig. 4a and Supplementary Fig. 4A–B), which is in agreement with previously reported results^{5,25}. Moreover, when these drugs were added after the fingers had formed, the traction force profile changed markedly (Fig. 4b,c). In particular, when using Y27632, the force at the leader cell became clearly negative (Fig. 4b), indicating that the leader cell had switched from pulling its followers to being pushed by them. In contrast, the Rac GEF inhibitor NSC 23766 had very limited influence on the migration of the monolayer (the average velocity and morphology of the border remained the same; Fig. 4a and Supplementary Fig. 4A), suggesting that Rac1 activation is not crucial in this process. We therefore conclude that the mechanism underlying finger development is mainly under RhoA control.

By analysing motile MDCK cells expressing the FRET biosensor Raichu-RhoA (RhoA^{Cter}) or Raichu-Rac1 (Rac1^{Cter}), we could dynamically map the activity of these GTPases within the fingers. Here, we took advantage of the relatively low transfection efficiency (typically 5% of the cells) to image individual fluorescent cells within a majority of ones that were not fluorescent. The flat and extended lamellipodia of the leaders in which cyan fluorescent protein (CFP) intensity was too low were excluded from the analysis. Raichus are sensors of the presence of GEF activity (or of a positive GEF/GAP balance), not of RhoA or Rac1 localization nor of endogenous GTP-bound RhoA or Rac1. A limitation is that Raichus cannot completely reflect the physiological RhoA or Rac1 localization for various reasons, including their incapacity to bind to guanosine nucleotide dissociation inhibitors, which play an important role in the cytosol-membrane shuttling of Rho GTPases. Nevertheless, it is commonly accepted that a positive GEF/GAP balance detected by Raichus mirrors an increased activity of endogenous RhoA or Rac1 (ref. 33).

Live FRET confocal microscopy about the basal plane showed that RhoA activity primarily localizes within 2 μm of the plane

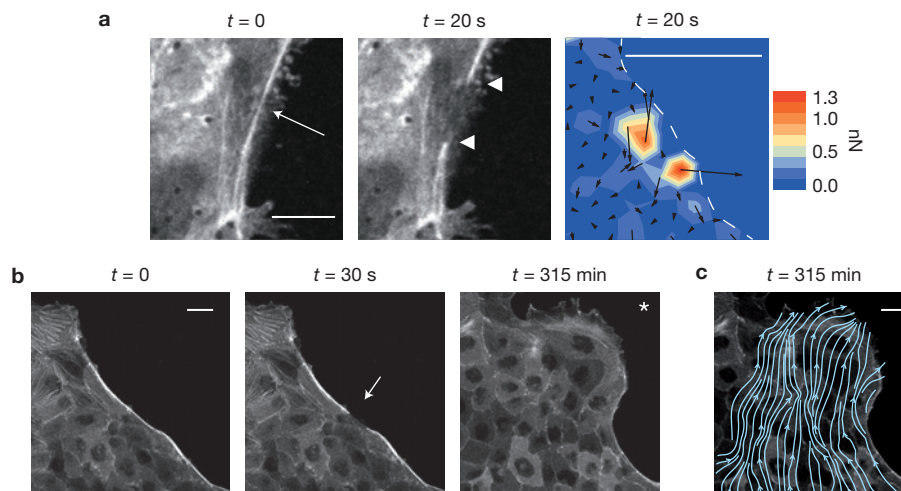


Figure 3 The contractile acto-myosin cable controls the initiation of new leader cells. **(a)** When cut by laser photoablation (arrow), the cable retracts rapidly (the extremities of the severed cable are denoted by the two triangles after 20 s; see also Supplementary Fig. 2A,B), which indicates that it is under tension. GFP-actin, scale bar, 10 μ m. This retraction is accompanied by local traction forces on the surface demonstrating the strong coupling of this cable to the substrate (Supplementary Fig. 2C). Representative images of > 20 replicates. **(b)** The ablation of the cable triggers the appearance of a new leader cell, demonstrating its 'confinement' function in preventing the

onset of new leaders. The arrow shows the point of laser ablation, and the asterisk is next to the new leader cell that starts to develop at this ablation point on the cable. GFP-actin, scale bar, 20 μ m. **(c)** The flow lines that show the direction of displacements were obtained from the mapping of the whole displacement field by particle image velocimetry as described in ref. 2. Each flow line is tangent to the local velocity at any point. Their high directionality over the whole finger that extends within the epithelium unambiguously identifies these structures as migration fingers (see Supplementary Movie 2). Representative images of 20 replicates.

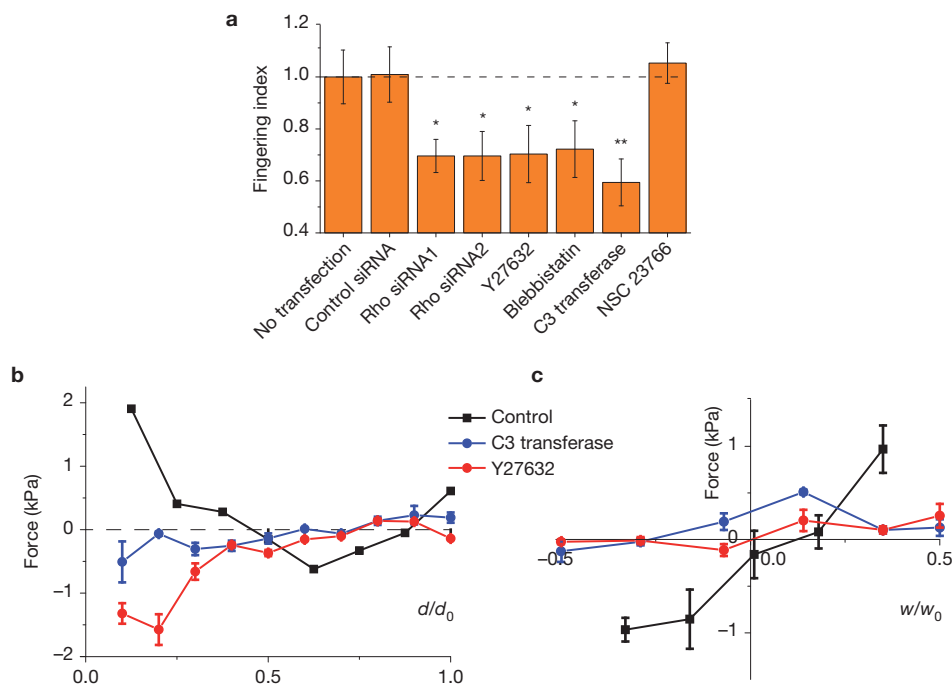


Figure 4 The force profiles under the fingers are under RhoA control. **(a)** Fingering index (root mean square distance between the actual profile and the line figuring its average position). Fingering index values have been normalized to the control value. Inhibitors against RhoA as well as siRNAs directed against RhoA show a significant decrease of the fingering index whereas the Rac1 inhibitor does not (see also Supplementary Fig. 4). Each bar results from averaging 6 distinct experiments. Error bars are s.e.m. (* $P < 0.05$; ** $P < 0.001$. Two-sample t -test). **(b,c)** Evolution of the traction forces developed by well-formed fingers following the addition of RhoA

inhibitors. Forces were measured 30 min to 2 h after addition of the inhibitor. **(b)** Longitudinal forces: a decrease (C3 transferase) and even an inversion (Y27632) of the force profile is seen following the addition of Rho inhibitors to a well-established finger. The phenotype close to the tip ($d/d_0 < 0.2$) switches from pulling the followers (positive forces) for the control, to being 'pushed' by them when Rho is inhibited by Y27632 (negative forces). $n=3$ fingers from 2 independent experiments. Error bars are s.e.m. **(c)** The transverse forces sharply decrease to very small values following the addition of the inhibitors. $n=3$ fingers from 2 independent experiments. Error bars are s.e.m.

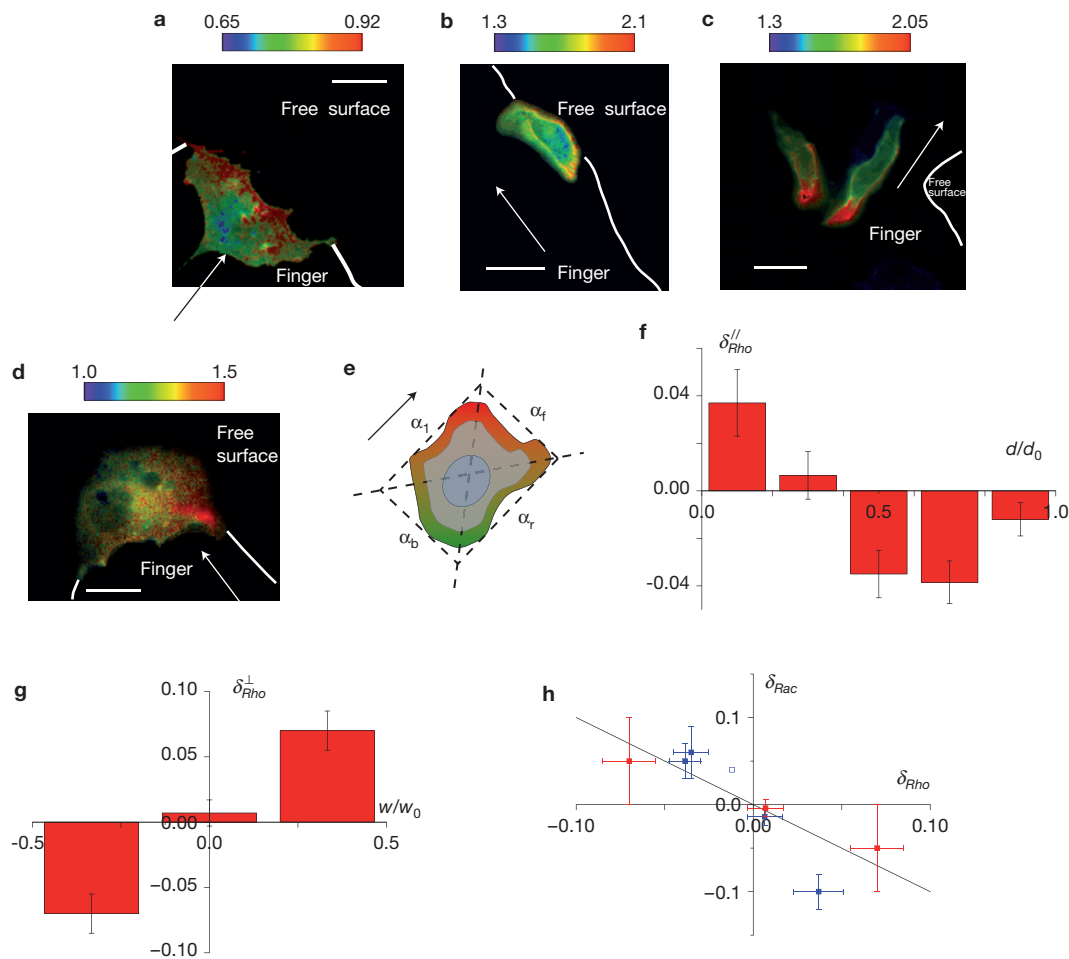


Figure 5 Mapping of RhoA and Rac1 differential activities within migration fingers. **(a–c)** Examples of the distribution of RhoA activity at the basal plane at several locations within a finger. For a leader cell, RhoA activity is highest at the front edge **(a)**. The distribution is inverted for cells closer to the epithelium **(c)**. Cells next to the acto-myosin cable have increased RhoA activity on the side adjacent to this cable **(b)**. The arrow is parallel to the finger axis and points towards the leader cell. **(d)** Rac1 differential activity at the leader cell. Note the decreased activity at the front of the leader cell compared with its rear (note that the cell immediately behind is not labelled). As for RhoA analysis, the low-fluorescence flat lamellipodium is excluded from the FRET analysis. Scale bars, 10 μm . (Representative images in **a**, **d**: 3 replicates; **b**, **c**: more than 20 replicates). **(e)** Definition of the differential activity. The arrow denotes the direction of migration of the cell. The activities α_x at the front, back, left and right are defined by the quadrants of the rectangle parallel to the direction of migration (arrow).

for the finger cells and at the top of the lamella for the leader cells (Supplementary Fig. 5). FRET confocal and non-confocal wide-field microscopies gave similar results (Fig. 5a–c and Supplementary Fig. 5): on the sides of the fingers, RhoA activity co-localized with the actin cable as previously mentioned (Fig. 5b and Supplementary Fig. 5B); and at the front side of the leader cells, most of the activity localized at the lamella²⁴ (Fig. 5a and Supplementary Fig. 5A), where we independently observed a high concentration of phospho-myosin light chain (Fig. 2c). Farther away from the tip of the finger, the activity was more localized at the cell rear-side (Fig. 5c and Supplementary Fig. 5C).

These quantities are used in the calculation of the differential activities as defined in the text. To exclude the spurious activity next to the nucleus, only the region next to the cell border is taken into account (width 0.6 μm). **(f)** Evolution of the longitudinal Rho differential activity along an ‘average finger’ obtained by binning and averaging ($n=30$ cells from 7 independent experiments). Error bars are s.e.m. **(g)** Transverse differential activity of Rho across the finger ($n=20$ cells from 5 independent experiments). Error bars are s.e.m. Note the same evolution as the corresponding force (Fig. 1d,e). **(h)** Relationship between the differential activities of RhoA and Rac1 for cells identically positioned within a finger in normalized coordinates. Blue points: longitudinal activities; red points: transverse activities. The line has a slope (–1) and illustrates the anticorrelation between these two quantities. $n=42$ cells from 10 independent experiments for Rho activity measurements, $n=20$ cells from 5 experiments for Rac activity measurements. Error bars are s.e.m.

To compare these results with the observed mechanical forces requires the activity gradient of the GTPases to be quantified at the cellular scale. Consequently, we defined the cells’ differential activities along the direction of the finger as³⁴: $\delta_{GP}^f = (\alpha_{GP}^f - \alpha_{GP}^b) / (\alpha_{GP}^f + \alpha_{GP}^b)$, where α_{GP}^x denotes the local subcellular activity of the G protein of interest (that is, RhoA or Rac1) at the cell front ($x=f$) and back ($x=b$) (Fig. 5e). Similar expressions were derived for δ_{GP}^l for the left–right activities. This last quantity was symmetrized about the finger axis. Rac1 and RhoA differential activities were a function of the position of the cells within the fingers (Fig. 5f,g and Supplementary Movies 3–5).

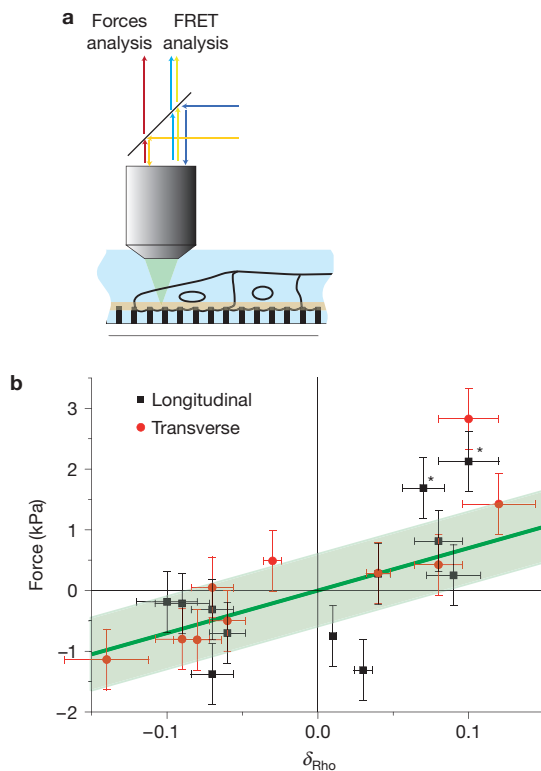


Figure 6 Traction forces and Rho differential activity are directly correlated. (a) Experimental set-up that allows the traction forces (red channel) and the FRET signal (yellow and cyan channels) to be measured on the same cells. Both signals were successively co-registered at the basal plane (orange slice) with an upright confocal microscope. (b) The total force developed by a given cell plotted against the corresponding differential activity (one point corresponds to one cell). δ_{Rho} and the force are of the same sign and proportional to each other. The same trend is confirmed on an averaged finger by accumulating data collected on independent fingers (Supplementary Fig. 6). The asterisks indicate leader cells. Error bars are experimental uncertainties. $n=12$ cells from 3 independent experiments.

Interestingly, by comparing cells located at the same normalized position, we found that δ_{Rho} and δ_{Rac} were quantitatively exactly anticorrelated in both directions within the limits of our experimental precision (Fig. 5h).

At the front edge of the leader cell body, we observed high levels of RhoA activity (Fig. 5a) and low Rac1 activity (Fig. 5d). These distributions complement the previously reported enhancement of the activities of these proteins at the leading edge of the lamellipodium^{16,33,35,36}, which we did not include in our analysis because of low expression levels of the biosensors. Our data thus highlight again the central role of the leader cell's lamella that seems to be under RhoA control³⁶. The transverse distribution of RhoA activity is maximum at the edges of the fingers, which reflects the co-localization of this GTPase with the acto-myosin cable³⁷.

Notably, leader cells are clearly not predetermined by an intrinsic RhoA polarity. When still in the monolayer, cells that eventually become leaders are initially characterized by a close-to-zero δ_{Rho} . As the finger forms and the phenotype of these cells changes to that of a leader, the gradient of Rho activity across the cell and the global force distribution both develop in parallel over a timescale of a few hours (Supplementary Fig. 3B,C). The formation and maintenance of these migration fingers therefore involve different roles for RhoA (ref. 21).

The supracellular distribution of RhoA activity mirrors the cartography of forces

When plotted against the normalized finger length or width, δ_{Rho} showed the same spatial variations as the mechanical forces that we measured and, in particular, the same sign change (Fig. 5f versus 1d, Fig. 5g versus Fig. 1e). Confocal observations performed directly on the fingers progressing on the micro-pillars showed a spatial localization of the RhoA FRET signal close to the basal plane where the traction forces are exerted (Fig. 6a and Supplementary Fig. 5). Moreover, inhibiting RhoA with C3 transferase resulted in a marked decrease in RhoA differential activity all along the finger, which mirrors the decrease in the force profile undersimilar conditions (Fig. 4b and Supplementary Fig. 4C). We therefore conclude that there is a strong direct correlation between Rho activity and the traction forces.

Indeed, there is a clear relationship between these quantities as shown in Fig. 6b, in which we plot the force developed by a given cell within the finger versus its RhoA differential activity measured in the plane corresponding to the top of the pillars. The traction forces were proportional to RhoA differential activity with a sensitivity (that is, the proportionality constant) of 7 ± 2 kPa (Fig. 6b). Concatenating data obtained by wide-field fluorescence microscopy on an 'average finger' confirmed that δ_{Rho} is proportional to the generated force with the same sensitivity as the confocal direct measurements (Supplementary Fig. 6).

DISCUSSION

Taking all these data together, we have shown that the fingers behave as mechanical global entities, with the leader cell dragging its followers by the large force it develops. The transmission of the forces within the structure establishes a tissue-scale coherent force profile and sets the peripheral actin cable under tension. Moreover, this supracellular mechanical organization corresponds to local gradients of RhoA activity at the level of the individual cells that constitute the finger. The striking correlation between the differential activity of RhoA and the local force clearly shows that this particular protein controls the migration fingers through active contractility. This relationship between tension, actin superstructures and Rho activation is yet another example of the transposition of concepts that have been validated on single cells³⁸ to the multicellular scale.

The importance of pluricellular peripheral acto-myosin contractile structures for the cohesion of pluricellular clusters has been underlined in two- and three-dimensional environments^{21,39}. By analogy, we propose that the cable discussed in the present study mechanically prevents the initiation of new leader cells within an already formed finger and therefore ensures the development of long migration fingers. The co-localization of RhoA activity with the cable illustrates again the strong correlation between this protein and mechanical forces. Previous observations have convincingly demonstrated the activation of RhoA by mechanical tension^{40,41}. We reason that this locally increased RhoA activity may in turn act positively on the contractility of the cable. Therefore, the force exerted by the leader cell on the whole structure induces a mechanical positive feedback loop on the cable tension through Rho activation. By this mechanism, a pluricellular coherent structure thus emerges, based on the spatial distribution of Rho activity at the level of single cells.

Migration fingers behave as mechanical global entities ('super-cells'). The interplay between the mechanical forces exerted by the cells during their collective migration and the local RhoA activity points to the importance of the acto-myosin cable in the formation and maintenance of the migration fingers. As these *in vitro* structures encapsulate some of the characteristics of many collectively migrating structures, including those observed in invading epithelial tumours^{20,39}, a similar mechanism may also be involved in the collective invasion of cancer cells. □

METHODS

Methods and any associated references are available in the [online version of the paper](#).

Note: Supplementary Information is available in the [online version of the paper](#)

ACKNOWLEDGEMENTS

It is a pleasure to thank G. Duclos for his help in several experiments, the members of the Biology-Inspired Physics at Mesoscales group and D. Louvard (Institut Curie) for discussions and support, M. Matsuda (Kyoto University) for sharing with us the FRET plasmids and for a critical analysis of our data, and W. J. Nelson (Stanford University) for the GFP-modified cell lines. We thank the Institut Curie-CNRS Nikon Imaging Center and the BDD imaging centre and particularly V. Fraiser, O. Leroy and L. Sengmanivong for technical support. We gratefully acknowledge financial support from the C'nano Ile de France, the Association Christelle Bouillot, the Association pour la Recherche sur le Cancer, the Labex CelTisPhyBio and the Institut Curie Programme Incitatif et Coopératif 'Physique de la Cellule'.

COMPETING FINANCIAL INTERESTS

The authors declare no competing financial interests.

Published online at www.nature.com/doi/10.1038/ncb2917

Reprints and permissions information is available online at www.nature.com/reprints

- Wood, W. *et al.* Wound healing recapitulates morphogenesis in *Drosophila* embryos. *Nat. Cell Biol.* **4**, 907–912 (2002).
- Poujade, M. *et al.* Collective migration of an epithelial monolayer in response to a model wound. *Proc. Natl Acad. Sci. USA* **104**, 15988–15993 (2007).
- Rørth, P. Collective guidance of collective cell migration. *Trends Cell Biol.* **17**, 575–579 (2007).
- Friedl, P., Locker, J., Sahai, E. & Segall, J. E. Classifying collective cancer cell invasion. *Nat. Cell Biol.* **14**, 777–783 (2012).
- Omelchenko, T., Vasiliev, J. M., Gelfand, I. M., Feder, H. H. & Bonder, E. M. Rho-dependent formation of epithelial 'leader' cells during wound healing. *Proc. Natl Acad. Sci. USA* **100**, 10788–10793 (2003).
- Vitorino, P. & Meyer, T. Modular control of endothelial sheet migration. *Genes Dev.* **22**, 3268–3281 (2008).
- Friedl, P. & Gilmour, D. Collective cell migration in morphogenesis, regeneration and cancer. *Nat. Rev. Mol. Cell Biol.* **10**, 445–457 (2009).
- Hegerfeldt, Y., Tusch, M., Bröcker, E. & Friedl, P. Collective cell movement in primary melanoma explants: plasticity of cell–cell interaction, β 1-integrin function, and migration strategies. *Cancer Res.* **62**, 2125–2130 (2002).
- Lim, J. I., Sabouri-Ghomi, M., Machacek, M., Waterman-Storer, C. M. & Danuser, G. Protrusion and actin assembly are coupled to the organization of lamellar contractile structures. *Exp. Cell Res.* **316**, 2027–2041 (2010).
- Khalil, A. A. & Friedl, P. Determinants of leader cells in collective cell migration. *Integr. Biol.* **2**, 568–574 (2010).
- Mark, S. *et al.* Physical model of the dynamic instability in an expanding cell culture. *Biophys. J.* **98**, 361–370 (2010).
- Treppe, X. *et al.* Physical forces during collective cell migration. *Nat. Phys.* **5**, 426–430 (2009).
- Tambe, D. T. *et al.* Collective cell guidance by cooperative intercellular forces. *Nat. Mater.* **10**, 469–475 (2011).
- Reffay, M. *et al.* Orientation and polarity in collectively migrating cell structures: statics and dynamics. *Biophys. J.* **100**, 2566–2575 (2011).
- Ridley, A. J. Life at the leading edge. *Cell* **145**, 1012–1022 (2011).
- Pertz, O., Hodgson, L., Klemke, R. L. & Hahn, K. M. Spatiotemporal dynamics of RhoA activity in migrating cells. *Nature* **440**, 1069–1072 (2006).
- Kaunas, R., Nguyen, P., Usami, S. & Chien, S. Cooperative effects of Rho and mechanical stretch on stress fiber organization. *Proc. Natl Acad. Sci. USA* **102**, 15895–15900 (2005).
- Theveneau, E. *et al.* Collective chemotaxis requires contact-dependent cell polarity. *Dev. Cell* **19**, 39–53 (2010).
- Wang, X., He, L., Wu, Y. I., Hahn, K. M. & Montell, D. J. Light-mediated activation reveals a key role for Rac in collective guidance of cell movement *in vivo*. *Nat. Cell Biol.* **12**, 591–597 (2010).
- Gaggioli, C. *et al.* Fibroblast-led collective invasion of carcinoma cells with differing roles for RhoGTPases in leading and following cells. *Nat. Cell Biol.* **9**, 1392–1400 (2007).
- Omelchenko, T. & Hall, A. Myosin-IXA regulates collective epithelial cell migration by targeting RhoGAP activity to cell–cell junctions. *Curr. Biol.* **22**, 278–288 (2012).
- Du Roure, O. *et al.* Force mapping in epithelial cell migration. *Proc. Natl Acad. Sci. USA* **102**, 2390–2395 (2005).
- Aoki, K. & Matsuda, M. Visualization of small GTPase activity with fluorescence resonance energy transfer-based biosensors. *Nat. Protoc.* **4**, 1623–1631 (2009).
- Burnette, D. T. *et al.* A role for actin arcs in the leading-edge advance of migrating cells. *Nat. Cell Biol.* **13**, 371–381 (2011).
- Farooqui, R. & Fenteany, G. Multiple rows of cells behind an epithelial wound edge extend cryptic lamellipodia to collectively drive cell-sheet movement. *J. Cell Sci.* **118**, 51–63 (2005).
- Saez, A., Bugni, A., Silberzan, P. & Ladoux, B. Is the mechanical activity of epithelial cells controlled by deformations or forces? *Biophys. J.* **89**, L52–L54 (2005).
- Dembo, M. & Wang, Y.-L. Stresses at the cell-to-substrate interface during locomotion of fibroblasts. *Biophys. J.* **76**, 2307–2316 (1999).
- Galbraith, C. G. & Sheetz, M. P. Keratocytes pull with similar forces on their dorsal and ventral surfaces. *J. Cell Biol.* **147**, 1313–1323 (1999).
- Fournier, M. F., Sauser, R., Ambrosi, D., Meister, J.-J. & Verkhovsky, A. B. Force transmission in migrating cells. *J. Cell Biol.* **188**, 287–297 (2010).
- Klarlund, J. K. Dual modes of motility at the leading edge of migrating epithelial cell sheets. *Proc. Natl Acad. Sci. USA* **109**, 15799–15804 (2012).
- Kumar, S. *et al.* Viscoelastic retraction of single living stress fibers and its impact on cell shape, cytoskeletal organization, and extracellular matrix mechanics. *Biophys. J.* **90**, 3762–3773 (2006).
- Hutson, M. S. *et al.* Forces for morphogenesis investigated with laser microsurgery and quantitative modeling. *Science* **300**, 145–149 (2003).
- Kurokawa, K. & Matsuda, M. Localized RhoA activation as a requirement for the induction of membrane ruffling. *Mol. Biol. Cell* **16**, 4294–4303 (2005).
- Eichorst, J. P., Lu, S., Xu, J. & Wang, Y. Differential RhoA dynamics in migratory and stationary cells measured by FRET and automated image analysis. *PLoS One* **3**, e4082 (2008).
- Machacek, M. *et al.* Coordination of Rho GTPase activities during cell protrusion. *Nature* **461**, 99–103 (2009).
- El-Sibai, M. *et al.* RhoA/ROCK-mediated switching between Cdc42- and Rac1-dependent protrusion in MTLn3 carcinoma cells. *Exp. Cell Res.* **314**, 1540–1552 (2008).
- Tamada, M., Perez, T. D., Nelson, W. J. & Sheetz, M. P. Two distinct modes of myosin assembly and dynamics during epithelial wound closure. *J. Cell Biol.* **176**, 27–33 (2007).
- Vaezi, A., Bauer, C., Vasioukhin, V. & Fuchs, E. Actin cable dynamics and Rho/Rock orchestrate a polarized cytoskeletal architecture in the early steps of assembling a stratified epithelium. *Dev. Cell* **3**, 367–381 (2002).
- Hidalgo-Carcedo, C. *et al.* Collective cell migration requires suppression of actomyosin at cell–cell contacts mediated by DDR1 and the cell polarity regulators Par3 and Par6. *Nat. Cell Biol.* **13**, 49–58 (2010).
- Zhao, X.-H. *et al.* Force activates smooth muscle alpha-actin promoter activity through the Rho signaling pathway. *J. Cell Sci.* **120**, 1801–1809 (2007).
- Lessey, E. C., Guilluy, C. & Burridge, K. From mechanical force to RhoA activation. *Biochemistry* **51**, 7420–7432 (2012).
- Bellusci, S., Moens, G., Thiery, J.-P. & Jouanneau, J. A scatter factor-like factor is produced by a metastatic variant of a rat bladder carcinoma cell line. *J. Cell Sci.* **107**, 1277–1287 (1994).
- Yamada, S., Pokutta, S., Drees, F., Weis, W. I. & Nelson, W. J. Deconstructing the cadherin-catenin-actin complex. *Cell* **123**, 889–901 (2005).
- Itoh, R. E. *et al.* Activation of rac and cdc42 video imaged by fluorescent resonance energy transfer-based single-molecule probes in the membrane of living cells. *Mol. Cell Biol.* **22**, 6582–6591 (2002).
- Yoshizaki, H. *et al.* Activity of Rho-family GTPases during cell division as visualized with FRET-based probes. *J. Cell Biol.* **162**, 223–232 (2003).
- Ghibaudo, M. *et al.* Traction forces and rigidity sensing regulate cell functions. *Soft Matter* **4**, 1836–1843 (2008).
- Hodgson, L., Nalbant, P., Shen, F. & Hahn, K. M. Imaging and photobleach correction of Mero-CBD, sensor of endogenous Cdc42 activation. *Methods Enzymol.* **406**, 140–156 (2006).
- Supatto, W. *et al.* *In vivo* modulation of morphogenetic movements in *Drosophila* embryos with femtosecond laser pulses. *Proc. Natl Acad. Sci. USA* **102**, 1047–1052 (2005).
- Rasband, W. S. *ImageJ v1.46b* (US National Institutes of Health, Bethesda, Maryland, 1997–2012).
- Deforet, M. *et al.* Automated velocity mapping of migrating cell populations (AveMap). *Nat. Methods* **9**, 1081–1083 (2012).
- Petitjean, L. *et al.* Velocity fields in a collectively migrating epithelium. *Biophys. J.* **98**, 1790–1800 (2010).

METHODS

Cell culture and reagents. The wild-type MDCK cell line is described in ref. 42. The actin–GFP MDCK cell line⁴³ was a generous gift from W. J. Nelson (Stanford University, USA). The cells were cultured in Dulbecco's modified Eagle's medium (DMEM) supplemented with 10% fetal bovine serum (Sigma), 2 mM L-glutamine solution (Gibco) and 1% antibiotic solution (penicillin; 10,000 units ml⁻¹), streptomycin (10 mg ml⁻¹; Gibco) at 37 °C, 5% CO₂ and 90% humidity throughout the experiments. Confocal imaging was performed in HEPES (Gibco) with temperature regulation alone.

Plasmids for the expression of the Raichu FRET probes for Rac1 (1,026 ×; ref. 44) and RhoA (1,298 ×; ref. 45) were gifts from M. Matsuda (Kyoto University, Japan). Using Lipofectamine 2000 (Invitrogen), MDCK cells were transiently transfected with the Raichu probes one night before being plated on the stencils.

The various inhibitors NSC 23766 (Tocris), Y27632 (Calbiochem), C3 transferase (Cytoskeleton) or blebbistatin (Sigma) were added 2 h before stencil removal or, when specified, after formation of fingers (4–6 h after stencil removal). We used concentrations of 50 μM for Y27632, 50 μM for blebbistatin, 1 μg ml⁻¹ for C3 transferase and 100 μM for NSC 23766.

Fibronectin (Invitrogen) was labelled with Cy5 (GE Healthcare) using the manufacturer's protocol to coat the top of the pillars for the force measurements.

Observations of the acto-myosin cable on fixed cells were performed with the actin–GFP or wild-type cell line. Cells were fixed with 4% paraformaldehyde, permeabilized with 0.1% Triton X-100 and incubated for 1 h with a rabbit phospho-myosin light chain 2 (Thr 18/Ser 19) antibody (Cell Signaling, #3674) diluted 1:200 in PBS supplemented with 10% FBS, and then for 1 h with a Cy3 donkey anti-rabbit antibody (BioLegend, number 406402) diluted 1:1,000 in the same medium. For double stainings with phalloidin, Alexa 488-conjugated phalloidin (Invitrogen; dilution 1:1,000) was added with the secondary antibody. Cells were then mounted on a coverslip using ProLong gold antifade reagent with DAPI (Invitrogen, Life Technologies).

siRNAs against RhoA were transfected using Lipofectamine RNAiMAX (Invitrogen): RhoA siRNA1, 5'-CCGGAAGAAACUGGUGAUU-3'; RhoA siRNA2, 5'-CCACAGUGUUUGAGAACA-3'.

For western blots, rabbit monoclonal 67B89 anti-RhoA (Cell Signaling number 2117; dilution 1:1,000) and mouse monoclonal 23A8 anti-Rac1 (Upstate number 05-389; dilution 1:1,000) were used.

Model wound assay. The assay consists of culturing cells in the apertures of a microfabricated openware film (stencil) until confluence at which point the stencil is removed and triggers the migration² (Supplementary Fig. 1A). In the present case, microstencils were made of polydimethylsiloxane (PDMS) elastomer (Sylgard 184, Dow Corning) and prepared by using photolithography and soft lithography techniques as described elsewhere². Briefly, 100-μm-thick rectangular prism structures were fabricated in negative photoresist (SU8-2100 or SU8-2050, Microchem) by conventional photolithography. This structure was replicated in PDMS by double moulding and then made non-adhesive by a plasma treatment followed by the reaction of a fluorosilane. To obtain the final microstencils, the last PDMS mould was placed on a clean PET film and uncured PDMS was allowed to penetrate the structure by capillary action for 3–4 h. The whole set-up was then cured at 65 °C for 48 h and the plastic film was peeled off. The microstencils were then carefully deposited on the surface (fibronectin-treated micropillar arrays or glass slides). Cells were plated in the apertures of the microstencils and cultured in the incubator until they reached confluence. At that time, the microstencils were gently peeled off. When used on micropillars, the medium was partially pumped out before plating the stencils so that the tops of the pillars showed on the surface of the medium.

When specified, inhibitors were added two hours before stencil removal. siRNA-treated cells were studied similarly 3 days after transfection.

Local force measurements. Force measurements were performed on dense arrays of vertical PDMS micropillars²² moulded from a silicon master obtained by classical microfabrication techniques. Most of the experiments were performed on a hexagonal array of 3-μm-high, 1-μm-diameter pillars (centre to centre distance was 2 μm). The corresponding substrates were obtained by moulding with PDMS a silicon master obtained by classical microfabrication techniques²². Briefly, the silicon wafers, etched by a deep reactive ion etching process, were moulded with PDMS. To allow for observations at high magnification, the thickness of the PDMS substrate supporting the pillars was controlled by using 80–120-μm-thick Nr. 0 coverslips (Menzel Glaser) as spacers. After 14 h at 65 °C, the PDMS was carefully peeled off in 70% ethanol to reduce the adhesion between pillars. Ethanol was then slowly exchanged with phosphate buffered saline (PBS; Gibco). The tops of the pillars were then treated with Cy5–fibronectin before the migration experiments by reverse microcontact printing with a flat PDMS stamp previously coated with the labelled protein⁴⁶.

The positions of the pillars were dynamically extracted from the fluorescence images acquired on an inverted IX71 microscope (Olympus) equipped with a 60× oil immersion objective, using home-made tracking software. Confocal imaging was performed on an upright confocal spinning-disc microscope (Zeiss, Roper) equipped with a 60× water-immersion objective. The fluorescent spots corresponding to the top of the pillars were fitted at sub-pixel resolution with a Gaussian function. Their displacements were measured relative to their position at rest calculated from the hexagonal lattice on a cell-free area. The number of posts analysed in each image was of the order of 1,000. The displacement vector Δx gives the force F through the expression:

$$F = k\Delta x; k = \frac{3}{4}\pi E \frac{r^4}{L^3}$$

where k is the spring constant and E , r and L are respectively the Young modulus, the radius and the length of the pillar. Numerically, $E \sim 2$ MPa (ref. 22), $r = 0.5$ μm, $L = 3$ μm and therefore $k = 11 \pm 1$ mN m⁻¹. A few experiments were also performed on 5-μm-high pillars (spring constant = 2.4 mN m⁻¹). The accuracy on the position at rest was limited by the large surface fraction covered by the epithelium. The estimated systematic error on the force was smaller than 0.5 nN. A total of 27 fingers were analyzed in 15 distinct experiments.

From these force maps, profiles of the projections of the two components of the forces were obtained by averaging in the corresponding direction. Forces in this analysis were also time-averaged over 4 h.

In the presence of inhibitors, forces were measured 1 h after the addition of Y27632 and 2 h after the addition of C3 transferase.

Time-lapse microscopy and image processing. Time-lapse wide-field images were acquired on an automated inverted microscope (Olympus IX71 or Nikon Eclipse TI) placed in a CO₂ incubator box (Life Imaging Service). Displacements of the stage (Prior Scientific), acquisitions with the CCD (charge-coupled device) camera (Retiga 4000, QImaging or EZ Coolsnap, Roper) and opening of the shutter (Uniblitz) were controlled through Metamorph (Universal Imaging). The delay between two successive frames was set between 5 and 20 min depending on the experiments. Experiments were performed for typically 24 h.

Raichu-transfected cells were imaged with the Olympus IX71 microscope equipped with a CFP/yellow fluorescent protein FRET filter set (86002v1JP4, Chroma Technology) and a ×60 oil-immersion objective. Images were acquired at the basal plane (depth of field ~ 2 μm). An antioxidant supplement (Sigma 1345) was added to the medium to minimize phototoxicity effect. Image frame rate was set between 15 and 45 min. Pseudocoloured ratio images were generated from images from the CFP and FRET channels as described previously⁴⁷ using Metamorph. The differential activities were measured in the basal plane as described in the text and in Fig. 5e.

Confocal imaging was performed on a temperature-controlled (LIS) upright confocal spinning-disc microscope (Zeiss, Roper) equipped with a CoolsnapHQ2 camera (Roper) and a ×60 water-immersion objective. In that case, a CFP/GFP FRET filter set was used (Fig. 6a). The experiment was computer-controlled with Metamorph. Slice thickness was fixed at 500 nm. In that case, no shading correction was used. The basal plane was defined as the top of the pillars. FRET activity was either measured at that plane or, when full stacks were acquired, averaged between that plane and the ones immediately above and below. Using this set-up, forces and FRET signal were dynamically measured successively on the same cells (Fig. 6a).

Photoablation experiments. Two-photon photoablation experiments were carried out on actin–GFP cells, at 37 °C in DMEM (Invitrogen) buffer, either on an Olympus IX71 or on a confocal Zeiss LSM 710 inverted microscope equipped with a ×63 high-numerical-aperture objective. We used a femto-second Ti:sapphire laser (MaiTai, Spectra Physics) operating between 80 and 150 mW at 920 nm (ref. 48). Microdissections (1 μm × 0.1 μm) consisted of a single line scan.

Data analysis. Forces were obtained from the deflections of the pillars that were measured using home-made software²². Data manipulation was performed using Igor (WaveMetrics) or Origin (OriginLab).

For the FRET analysis, images were acquired on the two channels; background was then subtracted using a cell-free area. No photobleaching effect was noticed as the fluorescence level remained constant over the experiment. Cells whose CFP signal was lower than a threshold were not included in the analysis. The ratio images were generated within the monolayer after masking by computing the FRET/CFP ratio pixel by pixel. These manipulations were performed using Matlab (MathWorks) or Igor (WaveMetrics) and ImageJ (ref. 49).

The differential activity measurements were performed by defining the rectangle that is both aligned with the cell displacement and fits best its shape (Fig. 5e). The spurious signal coming from the nucleus area was discarded by keeping only the first 0.6 μm next to the physical edge. Moreover, the flat low-fluorescence lamellipodium

was excluded from the FRET analysis. Forty-two cells in 10 independent experiments were studied for RhoA activity and 20 cells in 5 independent experiments for Rac1.

In Fig. 6b, forces and differential activities were measured simultaneously. In the other cases, quantitative comparisons of differential activities and forces were performed in parallel on cells identically localized within a finger after its normalization by its total length and total width. For better statistics, the values

were averaged in bins (typically 5 bins along the length and 3 bins across the width). At least 5 cells were counted in each bin.

When indicated, flow lines were calculated from the velocity field measured by particle image velocimetry⁵⁰ as described in ref. 51. These flow lines locally tangent the velocity at every point.

Unless otherwise noted, the error bars indicate the standard error of the mean (s.e.m.).

Interplay of RhoA and mechanical forces in collective cell migration driven by leader cells

M. Reay, M. C. Parrini, O. Cochet-Escartin, B. Ladoux, A. Buguin, S. Coscoy, F. Amblard, J. Camonis and P. Silberzan

Nat. Cell Biol. **16**, 217–223 (2014); published online 23 February 2014; corrected after print 26 February 2014

In the version of this Article originally published there were some errors:

The second citation of reference 1 in the first sentence of the main text should have been of reference 2 ('...or by the release of a physical barrier²...').

The present addresses of B. Ladoux were missing the area codes ('Paris F75205' and '117411 Singapore').

The caption of Fig. 1d–f should have read: '(d,e) Force profiles in the parallel and perpendicular directions resulting from averaging forces for 22 and 12 fingers from 15 and 10 independent experiments respectively. The thick red line is the average profile, the coloured area represents the standard deviation. (f) Schematic representation of the direction of the forces: the leader cell exerts a stable traction longitudinal force whereas the forces in the fingers are highly dynamic and can be positive or negative (red arrows). The side edges exert a centripetal force (green arrows). Fingers were composed of typically 30 cells.'

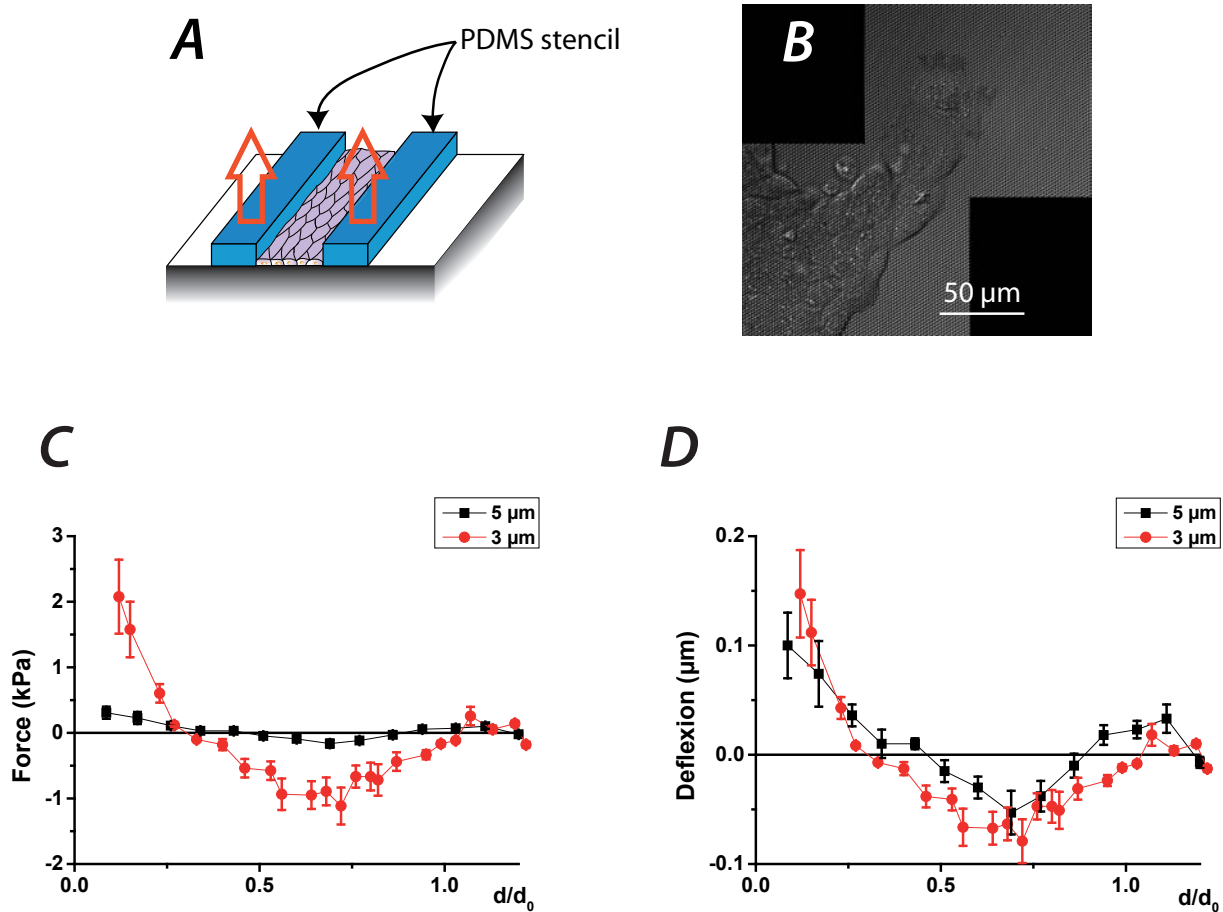
In the first sentence of the second paragraph under the heading 'Migration fingers are mechanical global entities', the figure citation should have read 'Fig. 1d,e'.

The first part of the caption of Fig. 3c should have read: '(c) The flow lines that show the direction...'

The citation of 'Supplementary Fig. 4C,B' in the first paragraph under the heading 'The supracellular distribution of RhoA activity mirrors the cartography of forces' should have read 'Fig. 4b and Supplementary Fig. 4C'.

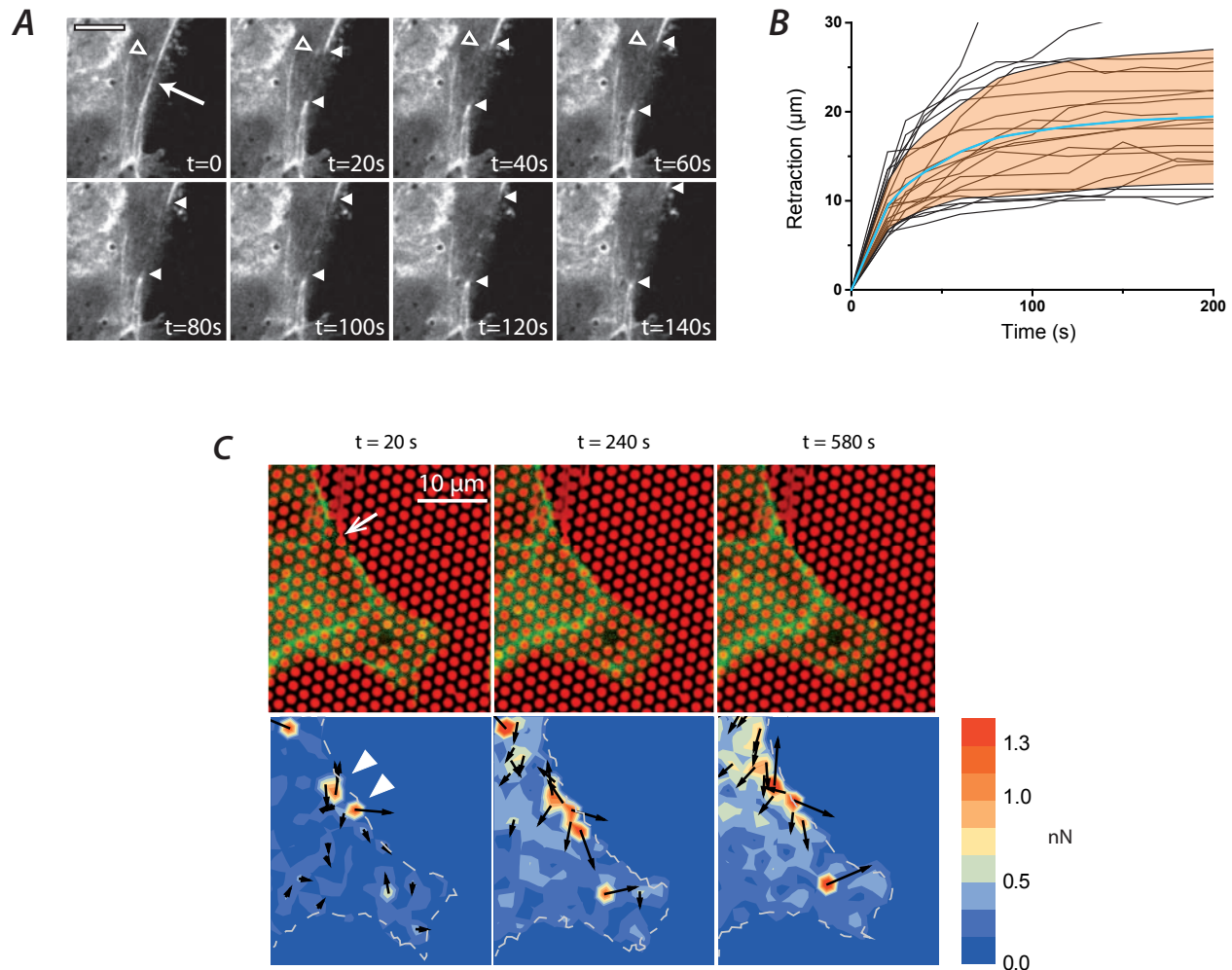
The page ranges for refs 17, 28, 44, 46 were missing; they are 15895–15900, 1313–1323, 6582–6591 and 1836–1843, respectively.

All these errors have been corrected in the online versions of the Article.



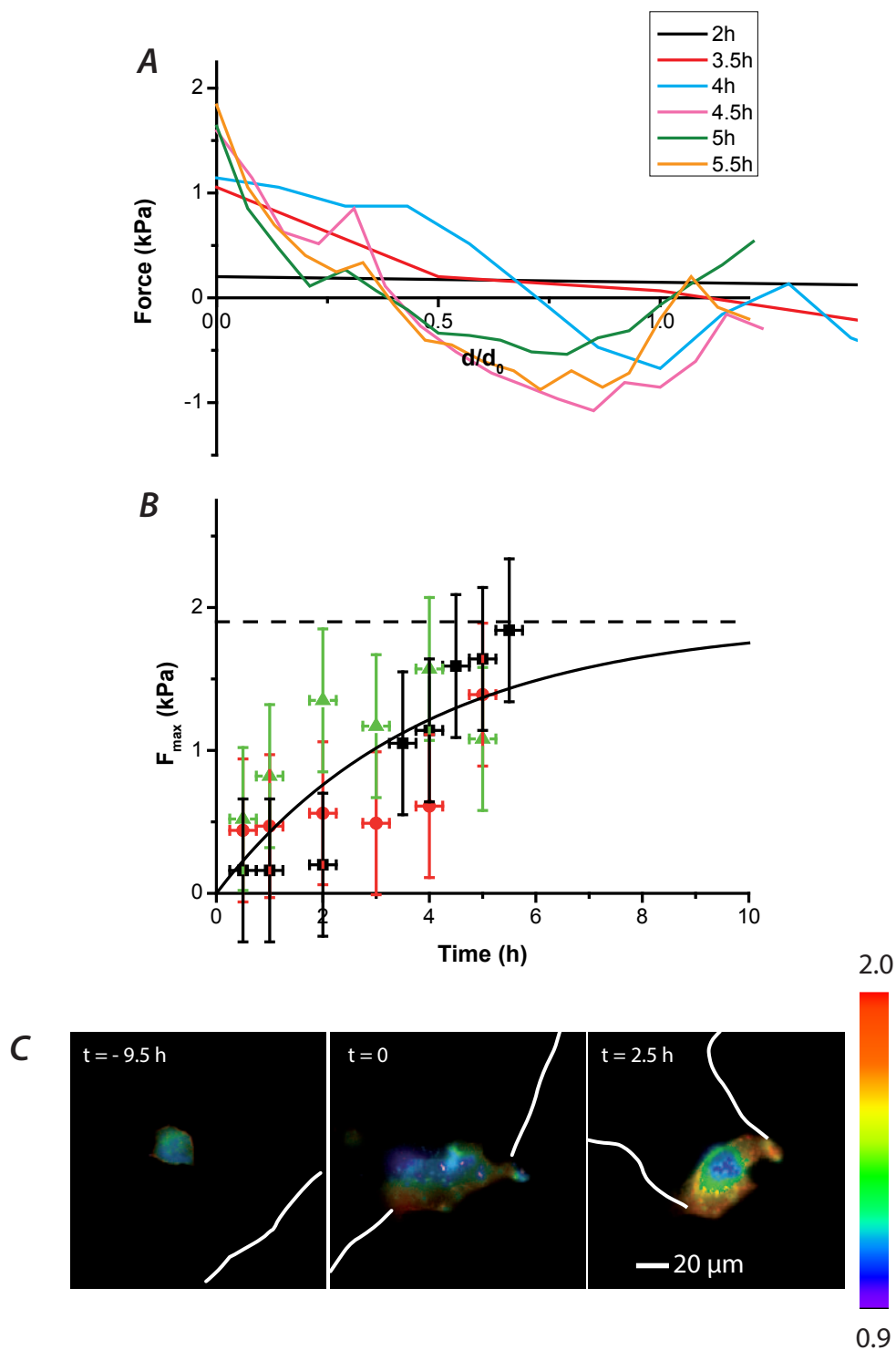
Supplementary Figure 1 Migration fingers respond to the micropillar array rigidity (A) Experimental set-up. The microstencil is deposited on the surface; cells are then seeded and cultured until confluence in the apertures. Peeling off the stencil triggers cell migration on the free surface. (B) Fingers develop well on a micropillar array. Phase contrast image of the migrating front on a micropillar array. The fingers are clearly identified. They are preceded by a leader cell of a specific phenotype. Representative image, more than 20 replicates. (C-D) Influence of the substrate rigidity on the force profile. (C)

Forces were measured on substrates differing on the height of the pillars and hence on their effective rigidity (see Material and Methods). The absolute forces were very different. (D) In contrast, the deflection of the pillars does not depend on their rigidity (i. e. the forces are proportional to the surface rigidity). 5 μm high pillars correspond to an effective Young Modulus of 1.7 kPa; 3 μm high pillars correspond to an effective Young modulus of 7.8 kPa¹. 5 μm -pillars: $n = 10$ fingers from 3 independent experiments; 3 μm -pillars: $n = 9$ fingers from 3 independent experiments. Error bars are SEMs.



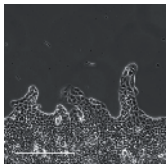


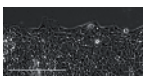
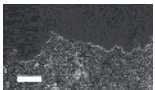
Supplementary Figure 2 The peripheral actin cable is under tension and interacts directly with the substrate **(A)** Image sequence following the severing of the actin-GFP cable by photoablation (scale bar 10μm). The white arrow indicates the initial ablation. The solid triangles denote the extremities of the retracting cable (see also Supp. Movie 1). Note that small structures next to the cable retract as well (empty triangle), demonstrating that this is a tension driven relaxation. Representative images. More than 20 replicates. **(B)** Distance between the two extremities of the cable as a function of time. The cyan line is the average of the different independent measurements (black curves), yielding a characteristic time of 37 ± 7 s

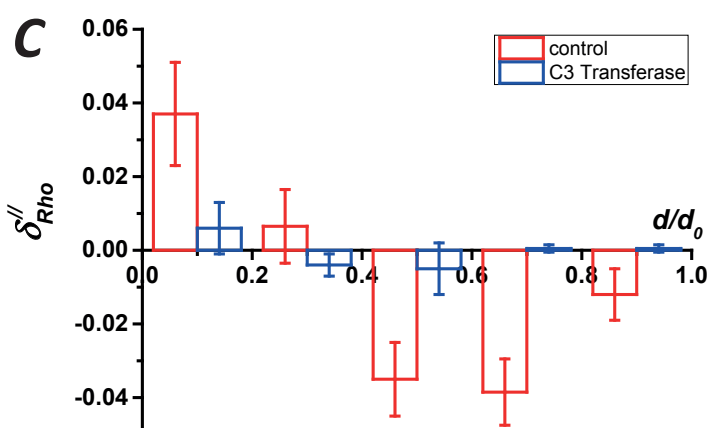
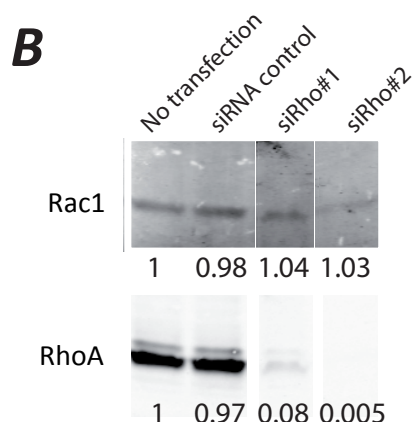
(SD) after a fit by an exponential function. The orange area is the standard deviation over 20 experiments. **(C)** When cut by photoablation (top panel, arrow), not only the forces at the cut relax but also the neighboring pillars situated under the cable. $t=0$ is the time of ablation. Top panel = actin-GFP and pillars – bottom panel = local forces (colours give the intensity and arrows the direction). The white triangles denote the high forces at pillars next to the cut. Note that the relaxation at longer times involves more pillars at a distance from the physical cut which demonstrates the direct interaction of the tensile actin cable with the substrate. Representative image. 20 replicates.



Supplementary Figure 3 Forces and RhoA distribution evolve with similar kinetics. A) Successive force profiles acquired after finger onset. $t=0$ represent the onset of the finger as visually determined. The profiles at early times are of smaller amplitude and shifted closer to the epithelium. B) Dynamic evolution of the force measured at the tip (coincides with the maximal force) for 3 fingers assessed from 3 independent experiments (one

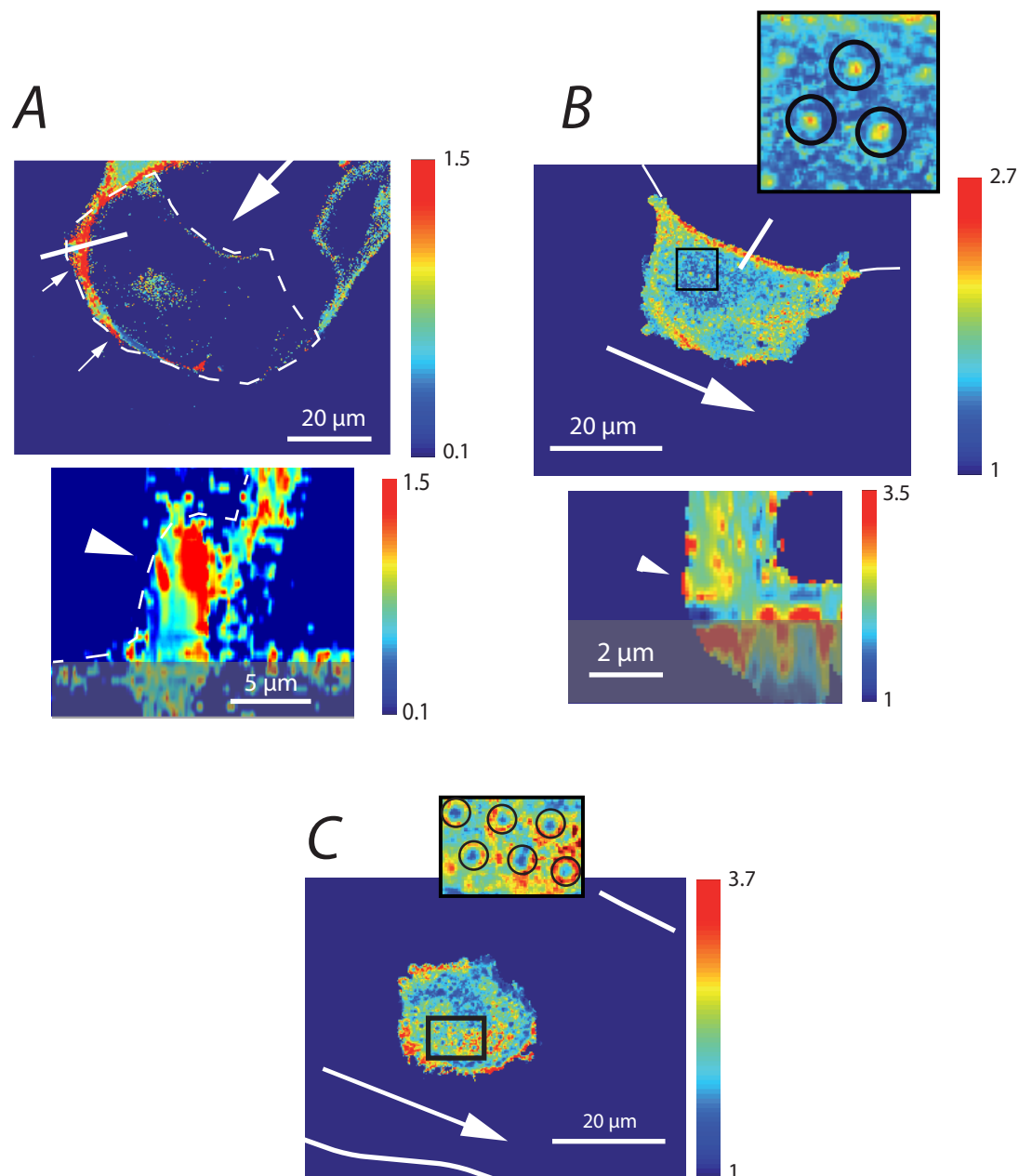
color stands for one finger), the line is an exponential fit of all the data. Error bars are the experimental absolute uncertainty. C) Representative cell becoming a leader within the epithelium (left), at the onset of the finger (center) and when the finger is fully developed (right). The gradient of RhoA activity in the leader cell sets up at similar time scales at the onset of a finger. Representative image. 3 replicates.

A	Control	ROCK Inhibitor (Y27632)²	Myosin inhibitor (Blebbistatin)³	RhoA inhibitor (C3-transferase)⁴	Rac GEF inhibitor (NSC23766)⁵
$t_0 + 20$ hrs					
Phenotype of fingers and leaders	Well-formed fingers, leader cells	no leader, no finger	short lived leaders (< 2hrs) Short fingers (< 70 μ m)	No leader, no finger (locally active protrusions)	Not different from control
Front velocity (μm/h)	11.2 ± 3.6	5.9 ± 1.3	14.6 ± 2.7	3.9 ± 1.1	9.5 ± 1.8
Action on preformed fingers	NA	Suppresses all leaders & fingers	Suppresses most of the fingers	Suppresses fingers	Not different from control



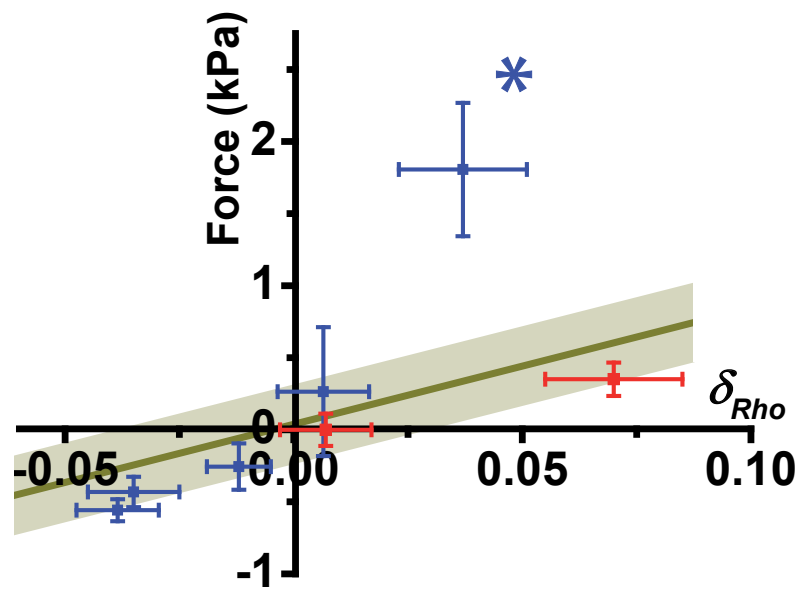
Supplementary Figure 4 Fingers are under RhoA control. **(A)** Use of chemical inhibitors. The drugs were used either at the beginning of the experiments or 4-6 hours after stencil removal to highlight their action on finger formation or on their maintenance. Leaders are identified by their phenotype (larger cells, active ruffling lamellipodium). Bars are 250 μ m. $n = 6$ independent experiments. Errors are SEMs. **(B)** Validation of anti-RhoA siRNAs. Western blots anti-Rac1 and anti-RhoA were performed on lysates of MDCK cells not-transfected or treated with control siRNA, siRhoA#1 or siRhoA#2. Expression levels were normalized towards

GAPDH (not shown) and the no-transfection condition was used as reference. **(C)** Distribution of RhoA differential activity along a finger in presence of C3 Transferase. The Rho inhibitor results in a strong decrease of δ_{Rho} (Blue). This decrease mirrors the response of the force profile in similar RhoA-inhibition conditions (Fig. 4B). Red points are the RhoA differential activity with no RhoA inhibition (from Fig. 5F). Observations were performed after 2hrs incubation of C3 transferase on $n = 16$ cells spanning 12 well-defined fingers from 2 independent experiments. Error bars are SEMs.



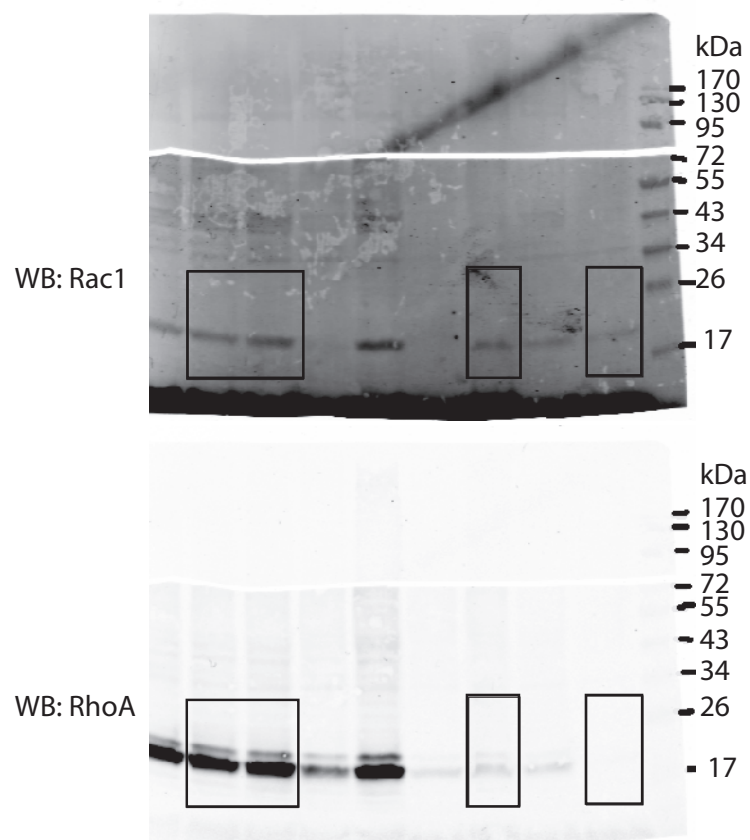
Supplementary Figure 5 Confocal imaging of RhoA activity for cells migrating on a micropillar array. In all the images, the large arrows point to the finger and points to the leader cell. **(A)** Leader cell: the high level of RhoA activity is highlighted by arrows and is colocalized with the lamella. In the xy image (top panel), the cell contour is outlined with a dashed line. This image is taken $\sim 4 \mu\text{m}$ above the tops of the pillars (triangle on the xz section (bottom panel)). The dashed line on the xz section outlines the lamella. **(B)** Enhancement of the activity at the free edge of the finger where it is colocalized with the actin cable. Top panel: xy section; bottom panel xz

section. In both **(A)** and **(B)** images, the xz section is taken along the white line of the corresponding xy image. The grey box at the bottom represents a volume below the top of the pillars where imaging is not reliable. **(C)** at the basis of the finger, the polarity is very weak (front side and backside activities are comparable). In images **(B)** and **(C)**, the top of the pillars are clearly apparent (insets). Note that image processing was optimized for FRET differences (colour differences), rather than biosensor localization (signal intensity). Representative images. 3-6 replicates from 3 independent experiments.



Supplementary Figure 6 Force-RhoA activity relationship. Force was plotted against d_{Rho} for cells identically positioned in a finger in normalized coordinates. This Figure is the equivalent of Fig. 6B for a normalized “average finger” derived from several independent experiments. Points have been binned according to their position along and across the fingers and average force and Rho activity values within these bins are reported

on this graph. Blue points: longitudinal direction, Red points: transverse direction. The line is the sensitivity as measured in the confocal plane (Fig. 6B). It describes well most of the points with the exception of the leaders (asterisk). Error bars are SEMs. Longitudinal direction: $n = 30$ cells assessed from 7 experiments. Transverse direction: $n = 20$ cells assessed from 5 experiments.



Supplementary Figure 7 Uncropped Western Blot with markers of Supplementary Figure 4B.

REFERENCES

1. Saez, A., Buguin, A., Silberzan, P. & Ladoux, B. Is the mechanical activity of epithelial cells controlled by deformations or forces? *Biophys. J.* **89**, L52–4 (2005).
2. Sutton, T. A., Mang, H. E. & Atkinson, S. J. Rho-kinase regulates myosin II activation in MDCK cells during recovery after ATP depletion. *Am. J. Physiol. Physiol.* **281**, F810 (2001).
3. Straight, A. F. et al. Dissecting temporal and spatial control of cytokinesis with a myosin II Inhibitor. *Science* **299**, 1743–7 (2003).
4. Gopalakrishnan, S., Raman, N., Atkinson, S. J. & Marrs, J. A. Rho GTPase signaling regulates tight junction assembly and protects tight junctions during ATP depletion. *Am. J. Physiol. Physiol.* **275**, C798 (1998).
5. Desai, R. a, Gao, L., Raghavan, S., Liu, W. F. & Chen, C. S. Cell polarity triggered by cell-cell adhesion via E-cadherin. *J. Cell Sci.* **122**, 905–11 (2009).

Supplementary Video Legends

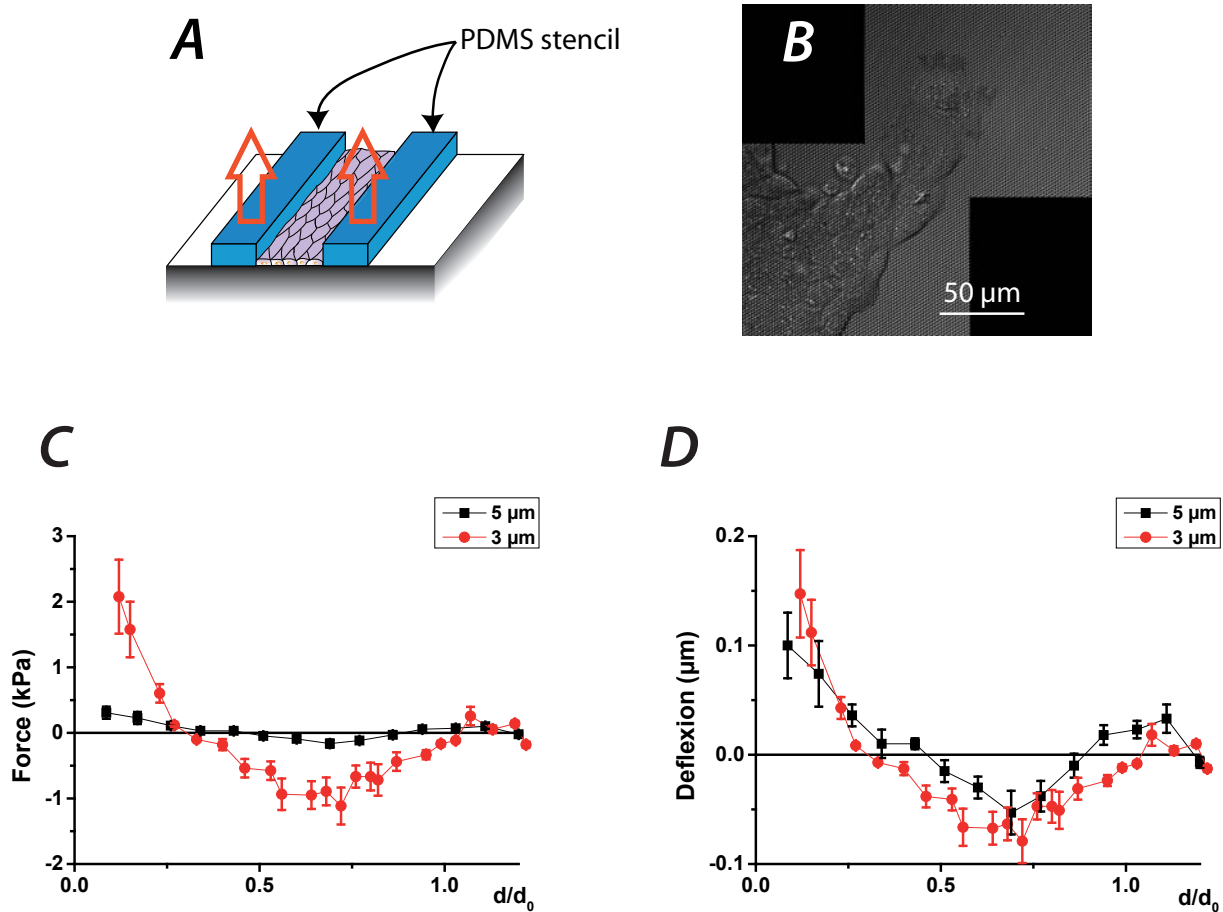
Supplementary Video 1 Retraction of the actin cable after photoablation. The actin-GFP MDCK cells forming a migration finger identical to the wild type cells. Two-photon laser photoablation severed the peripheral actin cable whose retraction indicates that it is under tension. Time interval is 30 s. Scale bar indicates 20 microns.

Supplementary Video 2 Onset of new leader at a weak point of the actin cable. After severing of the peripheral cable (see Supp. Movie 1), a new leader emerges at the exact point of ablation. Time delay is indicated on the right upper corner. Time interval is 15 min. Scale bar indicates 20 micron.

Supplementary Video 3 Distribution of RhoA activity in a leader cell preceding a finger. This cell is transfected with the RhoA biosensor. Note the higher RhoA activity at the front side of the leader compared to the backside.

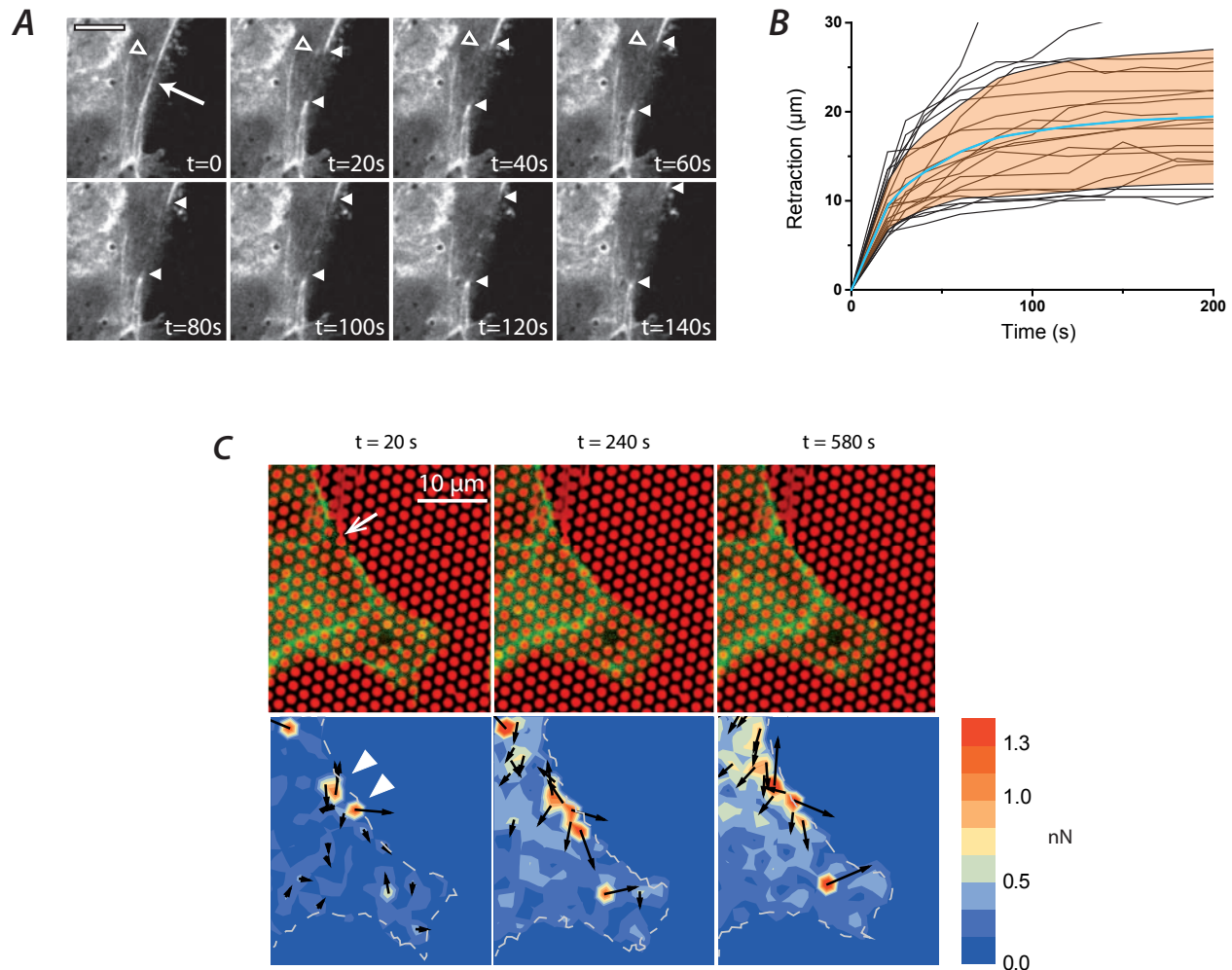
Supplementary Video 4 Distribution of RhoA activity in a finger cell close to the epithelium. This cell is transfected with the RhoA biosensor. Note the higher RhoA activity at the backside of the cell compared to its front side.

Supplementary Video 5 Distribution of Rac1 activity in a leader cell preceding a finger. This cell is transfected with the Rac1 biosensor. Note the higher Rac1 activity at the back side of the leader compared to its front side



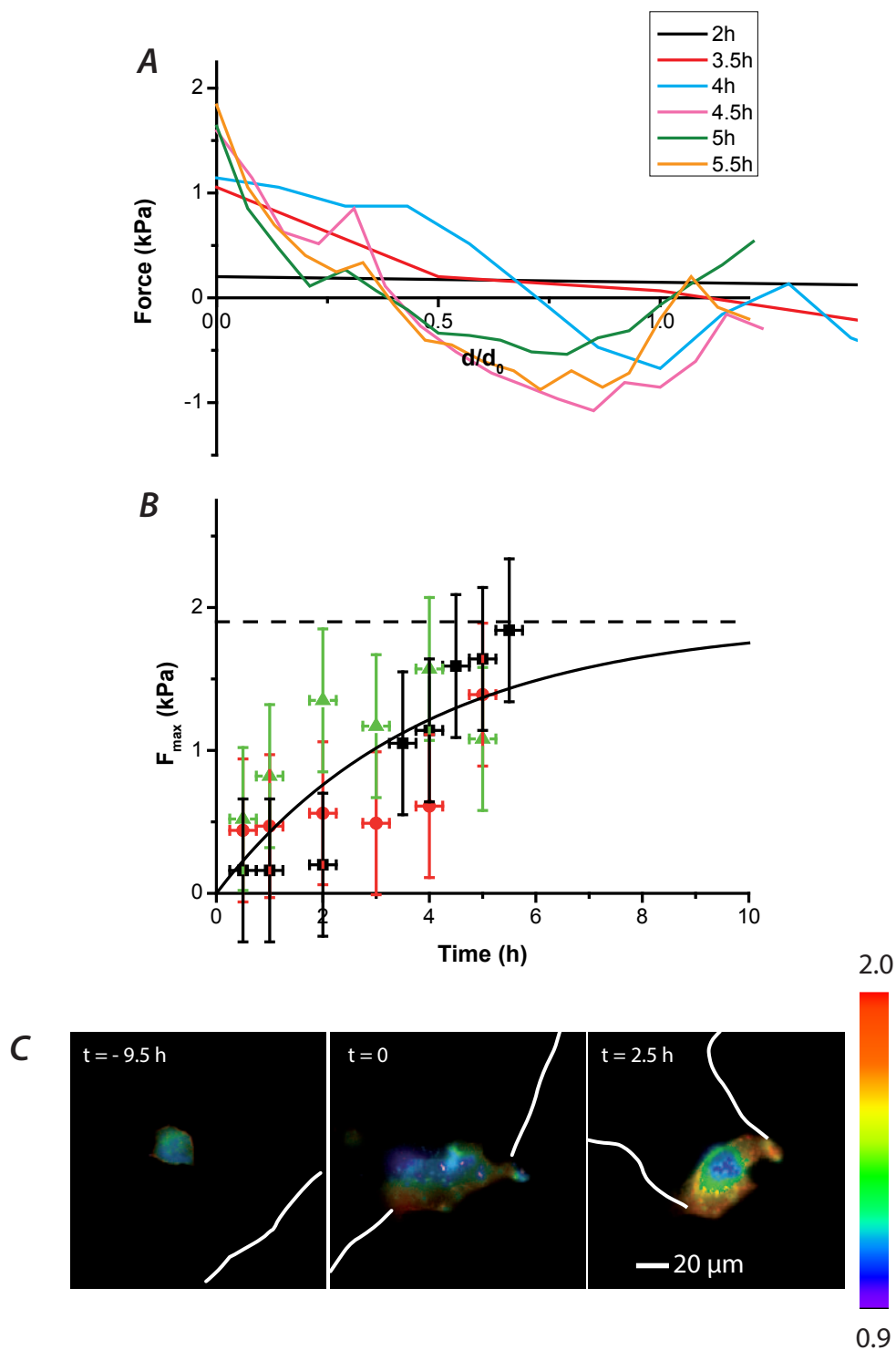
Supplementary Figure 1 Migration fingers respond to the micropillar array rigidity (A) Experimental set-up. The microstencil is deposited on the surface; cells are then seeded and cultured until confluence in the apertures. Peeling off the stencil triggers cell migration on the free surface. (B) Fingers develop well on a micropillar array. Phase contrast image of the migrating front on a micropillar array. The fingers are clearly identified. They are preceded by a leader cell of a specific phenotype. Representative image, more than 20 replicates. (C-D) Influence of the substrate rigidity on the force profile. (C)

Forces were measured on substrates differing on the height of the pillars and hence on their effective rigidity (see Material and Methods). The absolute forces were very different. (D) In contrast, the deflection of the pillars does not depend on their rigidity (i. e. the forces are proportional to the surface rigidity). 5 μm high pillars correspond to an effective Young Modulus of 1.7 kPa; 3 μm high pillars correspond to an effective Young modulus of 7.8 kPa¹. 5 μm -pillars: $n = 10$ fingers from 3 independent experiments; 3 μm -pillars: $n = 9$ fingers from 3 independent experiments. Error bars are SEMs.



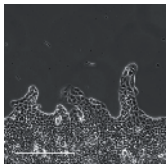
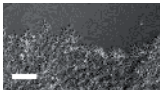
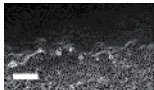
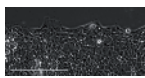
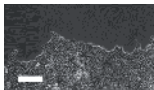
Supplementary Figure 2 The peripheral actin cable is under tension and interacts directly with the substrate **(A)** Image sequence following the severing of the actin-GFP cable by photoablation (scale bar $10\mu m$). The white arrow indicates the initial ablation. The solid triangles denote the extremities of the retracting cable (see also Supp. Movie 1). Note that small structures next to the cable retract as well (empty triangle), demonstrating that this is a tension driven relaxation. Representative images. More than 20 replicates. **(B)** Distance between the two extremities of the cable as a function of time. The cyan line is the average of the different independent measurements (black curves), yielding a characteristic time of 37 ± 7 s

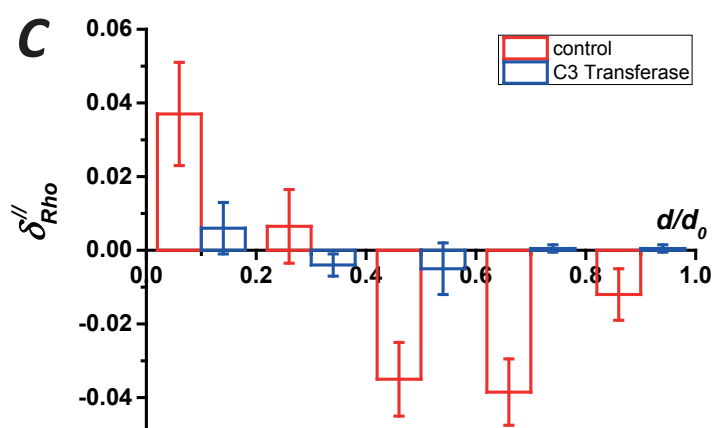
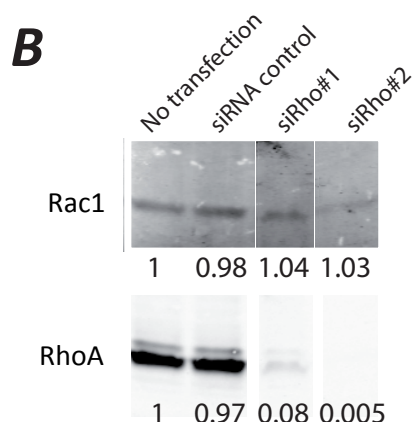
(SD) after a fit by an exponential function. The orange area is the standard deviation over 20 experiments. **(C)** When cut by photoablation (top panel, arrow), not only the forces at the cut relax but also the neighboring pillars situated under the cable. $t=0$ is the time of ablation. Top panel = actin-GFP and pillars – bottom panel = local forces (colours give the intensity and arrows the direction). The white triangles denote the high forces at pillars next to the cut. Note that the relaxation at longer times involves more pillars at a distance from the physical cut which demonstrates the direct interaction of the tensile actin cable with the substrate. Representative image. 20 replicates.



Supplementary Figure 3 Forces and RhoA distribution evolve with similar kinetics. A) Successive force profiles acquired after finger onset. $t=0$ represent the onset of the finger as visually determined. The profiles at early times are of smaller amplitude and shifted closer to the epithelium. B) Dynamic evolution of the force measured at the tip (coincides with the maximal force) for 3 fingers assessed from 3 independent experiments (one

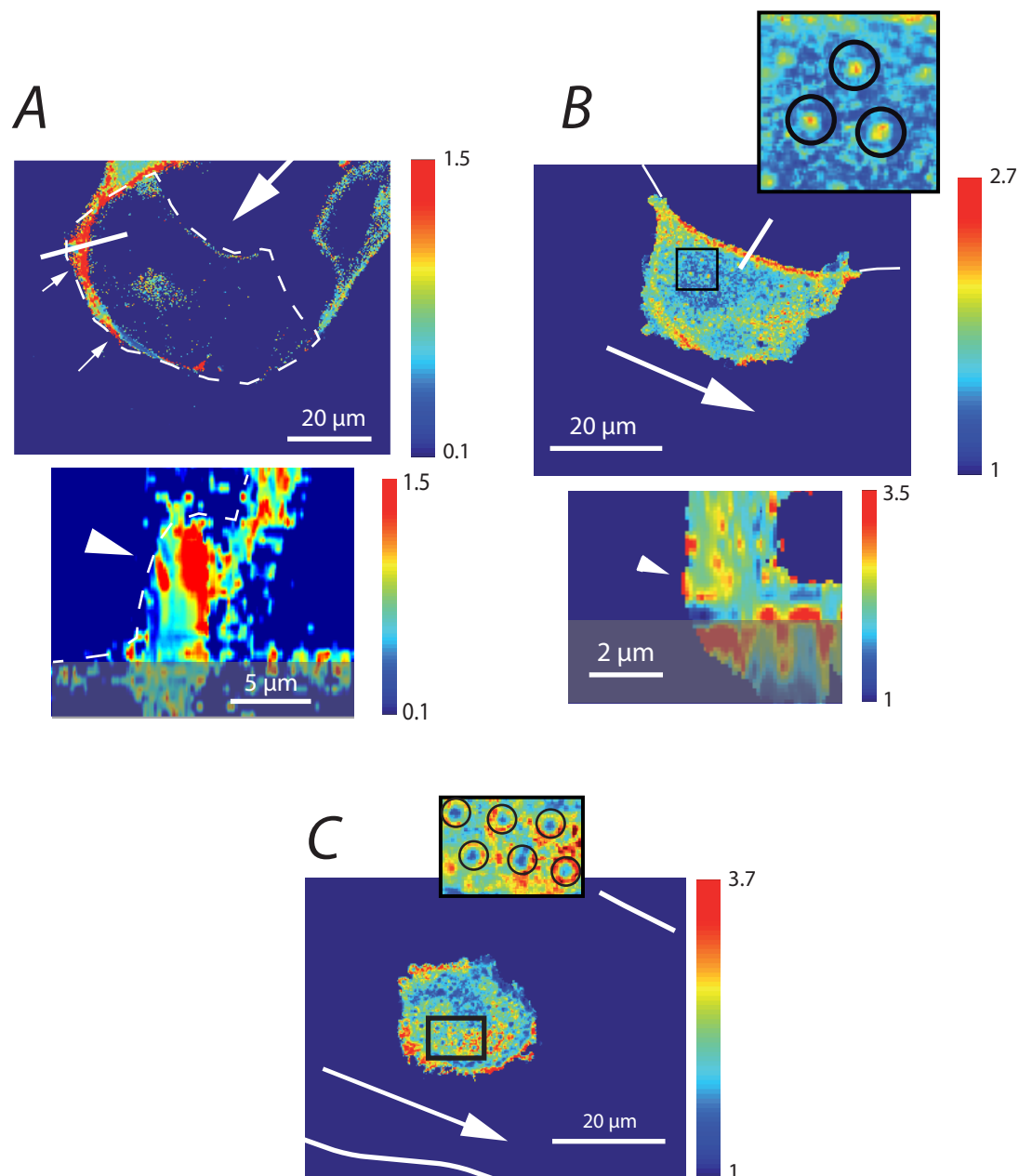
color stands for one finger), the line is an exponential fit of all the data. Error bars are the experimental absolute uncertainty. C) Representative cell becoming a leader within the epithelium (left), at the onset of the finger (center) and when the finger is fully developed (right). The gradient of RhoA activity in the leader cell sets up at similar time scales at the onset of a finger. Representative image. 3 replicates.

A	Control	ROCK Inhibitor (Y27632)²	Myosin inhibitor (Blebbistatin)³	RhoA inhibitor (C3-transferase)⁴	Rac GEF inhibitor (NSC23766)⁵
$t_0 + 20$ hrs					
Phenotype of fingers and leaders	Well-formed fingers, leader cells	no leader, no finger	short lived leaders (< 2hrs) Short fingers (< 70 μ m)	No leader, no finger (locally active protrusions)	Not different from control
Front velocity (μm/h)	11.2 ± 3.6	5.9 ± 1.3	14.6 ± 2.7	3.9 ± 1.1	9.5 ± 1.8
Action on preformed fingers	NA	Suppresses all leaders & fingers	Suppresses most of the fingers	Suppresses fingers	Not different from control



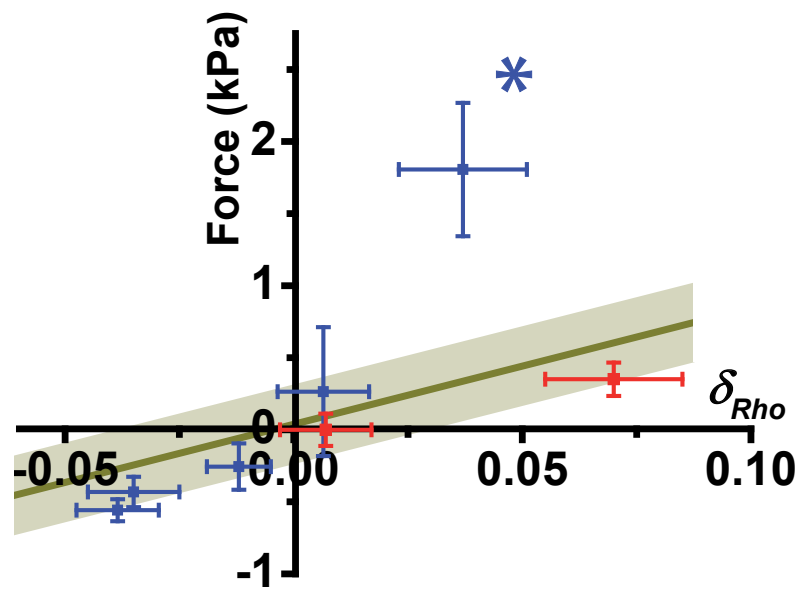
Supplementary Figure 4 Fingers are under RhoA control. **(A)** Use of chemical inhibitors. The drugs were used either at the beginning of the experiments or 4-6 hours after stencil removal to highlight their action on finger formation or on their maintenance. Leaders are identified by their phenotype (larger cells, active ruffling lamellipodium). Bars are 250 μ m. $n = 6$ independent experiments. Errors are SEMs. **(B)** Validation of anti-RhoA siRNAs. Western blots anti-Rac1 and anti-RhoA were performed on lysates of MDCK cells not-transfected or treated with control siRNA, siRhoA#1 or siRhoA#2. Expression levels were normalized towards

GAPDH (not shown) and the no-transfection condition was used as reference. **(C)** Distribution of RhoA differential activity along a finger in presence of C3 Transferase. The Rho inhibitor results in a strong decrease of δ_{Rho} (Blue). This decrease mirrors the response of the force profile in similar RhoA-inhibition conditions (Fig. 4B). Red points are the RhoA differential activity with no RhoA inhibition (from Fig. 5F). Observations were performed after 2hrs incubation of C3 transferase on $n = 16$ cells spanning 12 well-defined fingers from 2 independent experiments. Error bars are SEMs.



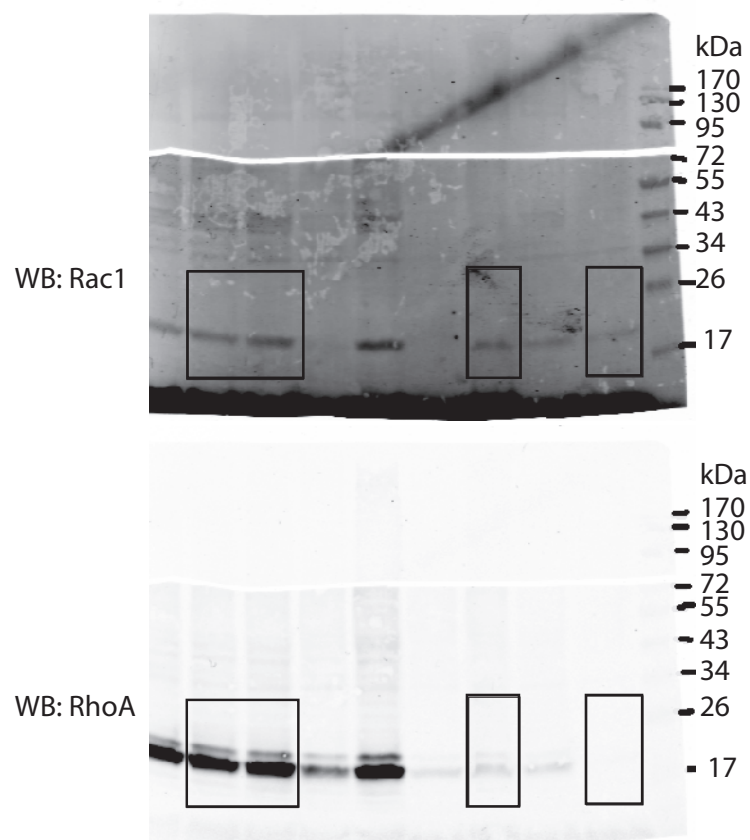
Supplementary Figure 5 Confocal imaging of RhoA activity for cells migrating on a micropillar array. In all the images, the large arrows point to the finger and points to the leader cell. **(A)** Leader cell: the high level of RhoA activity is highlighted by arrows and is colocalized with the lamella. In the xy image (top panel), the cell contour is outlined with a dashed line. This image is taken ~ 4 μm above the tops of the pillars (triangle on the xz section (bottom panel)). The dashed line on the xz section outlines the lamella. **(B)** Enhancement of the activity at the free edge of the finger where it is colocalized with the actin cable. Top panel: xy section; bottom panel xz

section. In both **(A)** and **(B)** images, the xz section are taken along the white line of the corresponding xy image. The grey box at the bottom represents a volume below the top of the pillars where imaging is not reliable. **(C)** at the basis of the finger, the polarity is very weak (front side and backside activities are comparable). In images **(B)** and **(C)**, the top of the pillars are clearly apparent (insets). Note that image processing was optimized for FRET differences (colour differences), rather than biosensor localization (signal intensity). Representative images. 3-6 replicates from 3 independent experiments.



Supplementary Figure 6 Force-RhoA activity relationship. Force was plotted against d_{Rho} for cells identically positioned in a finger in normalized coordinates. This Figure is the equivalent of Fig. 6B for a normalized “average finger” derived from several independent experiments. Points have been binned according to their position along and across the fingers and average force and Rho activity values within these bins are reported

on this graph. Blue points: longitudinal direction, Red points: transverse direction. The line is the sensitivity as measured in the confocal plane (Fig. 6B). It describes well most of the points with the exception of the leaders (asterisk). Error bars are SEMs. Longitudinal direction: $n = 30$ cells assessed from 7 experiments. Transverse direction: $n = 20$ cells assessed from 5 experiments.



Supplementary Figure 7 Uncropped Western Blot with markers of Supplementary Figure 4B.

REFERENCES

1. Saez, A., Buguin, A., Silberzan, P. & Ladoux, B. Is the mechanical activity of epithelial cells controlled by deformations or forces? *Biophys. J.* **89**, L52–4 (2005).
2. Sutton, T. A., Mang, H. E. & Atkinson, S. J. Rho-kinase regulates myosin II activation in MDCK cells during recovery after ATP depletion. *Am. J. Physiol. Physiol.* **281**, F810 (2001).
3. Straight, A. F. et al. Dissecting temporal and spatial control of cytokinesis with a myosin II Inhibitor. *Science* **299**, 1743–7 (2003).
4. Gopalakrishnan, S., Raman, N., Atkinson, S. J. & Marrs, J. A. Rho GTPase signaling regulates tight junction assembly and protects tight junctions during ATP depletion. *Am. J. Physiol. Physiol.* **275**, C798 (1998).
5. Desai, R. a, Gao, L., Raghavan, S., Liu, W. F. & Chen, C. S. Cell polarity triggered by cell-cell adhesion via E-cadherin. *J. Cell Sci.* **122**, 905–11 (2009).

Supplementary Video Legends

Supplementary Video 1 Retraction of the actin cable after photoablation. The actin-GFP MDCK cells forming a migration finger identical to the wild type cells. Two-photon laser photoablation severed the peripheral actin cable whose retraction indicates that it is under tension. Time interval is 30 s. Scale bar indicates 20 microns.

Supplementary Video 2 Onset of new leader at a weak point of the actin cable. After severing of the peripheral cable (see Supp. Movie 1), a new leader emerges at the exact point of ablation. Time delay is indicated on the right upper corner. Time interval is 15 min. Scale bar indicates 20 micron.

Supplementary Video 3 Distribution of RhoA activity in a leader cell preceding a finger. This cell is transfected with the RhoA biosensor. Note the higher RhoA activity at the front side of the leader compared to the backside.

Supplementary Video 4 Distribution of RhoA activity in a finger cell close to the epithelium. This cell is transfected with the RhoA biosensor. Note the higher RhoA activity at the backside of the cell compared to its front side.

Supplementary Video 5 Distribution of Rac1 activity in a leader cell preceding a finger. This cell is transfected with the Rac1 biosensor. Note the higher Rac1 activity at the back side of the leader compared to its front side

Interplay of RhoA and mechanical forces in collective cell migration driven by leader cells

M. Reay, M. C. Parrini, O. Cochet-Escartin, B. Ladoux, A. Buguin, S. Coscoy, F. Amblard, J. Camonis and P. Silberzan

Nat. Cell Biol. **16**, 217–223 (2014); published online 23 February 2014; corrected after print 26 February 2014

In the version of this Article originally published there were some errors:

The second citation of reference 1 in the first sentence of the main text should have been of reference 2 ('...or by the release of a physical barrier²...').

The present addresses of B. Ladoux were missing the area codes ('Paris F75205' and '117411 Singapore').

The caption of Fig. 1d–f should have read: '(d,e) Force profiles in the parallel and perpendicular directions resulting from averaging forces for 22 and 12 fingers from 15 and 10 independent experiments respectively. The thick red line is the average profile, the coloured area represents the standard deviation. (f) Schematic representation of the direction of the forces: the leader cell exerts a stable traction longitudinal force whereas the forces in the fingers are highly dynamic and can be positive or negative (red arrows). The side edges exert a centripetal force (green arrows). Fingers were composed of typically 30 cells.'

In the first sentence of the second paragraph under the heading 'Migration fingers are mechanical global entities', the figure citation should have read 'Fig. 1d,e'.

The first part of the caption of Fig. 3c should have read: '(c) The flow lines that show the direction...'

The citation of 'Supplementary Fig. 4C,B' in the first paragraph under the heading 'The supracellular distribution of RhoA activity mirrors the cartography of forces' should have read 'Fig. 4b and Supplementary Fig. 4C'.

The page ranges for refs 17, 28, 44, 46 were missing; they are 15895–15900, 1313–1323, 6582–6591 and 1836–1843, respectively.

All these errors have been corrected in the online versions of the Article.